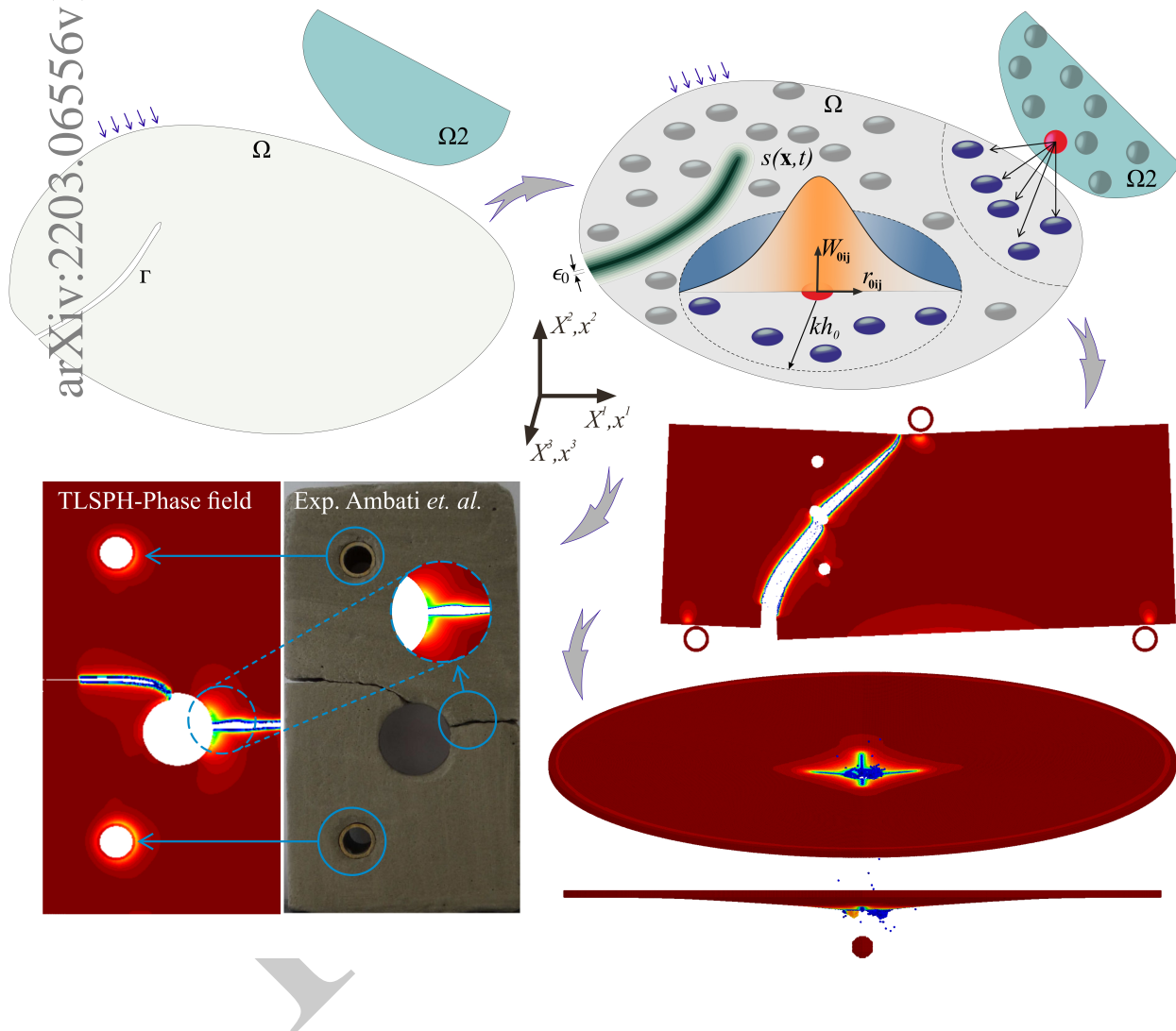


Graphical Abstract

A smoothed particle hydrodynamics approach for phase field modeling of brittle fracture

Mohammad Naqib Rahimi, Georgios Moutsanidis



Highlights

A smoothed particle hydrodynamics approach for phase field modeling of brittle fracture

Mohammad Naqib Rahimi, Georgios Moutsanidis

- Developed TLSPH-Phase field for brittle fracture simulations
- SPH is posed in a total Lagrangian framework to eliminate tensile instability
- Discontinuities are regularized over a length scale and are represented by the phase field parameter
- A hyperbolic version of the phase field governing equation is used to facilitate explicit time integration
- Challenging two and three dimensional problems with complex fracture patterns and contact are solved

A smoothed particle hydrodynamics approach for phase field modeling of brittle fracture

Mohammad Naqib Rahimi^a, Georgios Moutsanidis^{a,b,*}

^a*Department of Civil Engineering, Stony Brook University, Stony Brook, NY 11794, USA*

^b*Institute for Advanced Computational Science, Stony Brook, NY 11794, USA*

Abstract

Fracture is a very challenging and complicated problem with various applications in engineering and physics. Although it has been extensively studied within the context of mesh-based numerical techniques, such as the finite element method (FEM), the research activity within the Smoothed Particle Hydrodynamics (SPH) community remains scarce. SPH is a particle based method, ideal to simulate fracture scenarios that involve extreme deformations. However, to model fracture, SPH researchers have mostly relied on ad-hoc empirical local damage models, cohesive zone approaches, or pseudo-spring models, which come with a set of drawbacks and limitations. On the other hand, phase field models of brittle fracture have recently gained popularity in academic circles and provide significant improvements compared to previous approaches. These improvements include the derivation from fundamental fracture theories, the introduction of non-locality, and the ability to model multiple crack initiation, propagation, branching, and coalescence, in situations where no prior knowledge of the crack paths is available. Nevertheless, phase field modeling has not been combined with SPH for fracture simulations. In this proof-of-concept paper we develop and implement a phase field model of brittle fracture within the context of SPH. Comprehensive mathematical and implementation details are provided, and several challenging numerical examples are computed and illustrate the proposed method's ability to accurately and efficiently simulate complex fracture scenarios with the SPH framework.

Keywords: SPH; Particle methods; Phase field; Fracture mechanics; Non-local methods; Contact mechanics

1. Introduction

The Smoothed Particle Hydrodynamics (SPH) is one of the oldest and well established particle methods, and has an outstanding application history in many fields. SPH was originally developed

*Corresponding author

Email address: georgios.moutsanidis@stonybrook.edu (Georgios Moutsanidis)

as an interpolation technique to study astrophysics related problems [1, 2], and was later extended to model fluid mechanics [3]. One of the major advantages of SPH over other existing particle methods, is that the inclusion of new physics is quite straightforward, and it can therefore be readily extended to new areas of application [4]. When it comes to solid mechanics, its ability to handle extreme material distortion makes it ideal for simulating large deformation problems, where conventional Lagrangian mesh-based techniques fail due to mesh entanglement and the need for frequent mesh update or remeshing. Many interesting variants of the technique have been developed since its initial appearance, and the interested reader should consult [1–13] and the references therein.

Although SPH has been successfully applied to some complex problems in solid mechanics, fracture is still a challenging and open research area within the SPH community, and has not been extensively studied. This is because SPH is a continuum-based method and cannot, by its own, model fracture and distinct crack surfaces. SPH researchers have so far relied on ad-hoc empirical local damage models [14], pseudo-spring and virtual link approaches [15–17], cohesive zone models [18–20], and “cracking particles” approaches [21]. However, the above-mentioned techniques suffer from drawbacks and limitations. Local damage models are based on empirical damage laws rather than comprehensive fracture theories, and lead to mesh dependency and non-convergent results under refinement. The “cracking particles” approach resembles the extended finite element method (XFEM) [22, 23], therefore the fracture paths need to be predefined. In the pseudo-spring approach the damage evolution is based on rather simple linear damage models, the softening curve of the damage law might lead to instabilities, and past research has shown that they are prone to spurious damage patterns. Finally, in cohesive zone models there are a few tunable parameters for which there is not systematic way of derivation, the crack paths usually need to be known a-priori, and the fracture surfaces need to be tracked explicitly. Even though the aforementioned crack simulation techniques proved sufficient for certain classes of problems, it is evident that there is significant room for improvement when it comes to modeling fracture within the SPH framework.

Recently, phase field models of brittle fracture gained popularity within academic circles. Many interesting variants of the method have emerged and several challenging applications have been addressed [24–33]. In phase field for fracture, cracks are not explicitly introduced in the solid, but instead the fracture surface is approximated by a phase field parameter that diffuses the discontinuity over a small region. The phase field parameter represents the material integrity, and it is a continuous variable that describes the smooth transition from the fully intact to the fully damaged state. The evolution of phase field, and hence of the fracture surface, is governed by a partial differential equation (PDE). Thus, a degree of non-locality is introduced, since the damage state at one point depends (through derivative information) on the states of neighboring points.

The non-locality of the method leads to a well-posed mathematical model that exhibits mesh independence and convergence under refinement. At the same time, it can easily handle complicated discontinuity scenarios, such as crack initiation, propagation, coalescence, and branching, without prior knowledge of the crack paths, and without the need to embed any evolving discontinuities in the displacement field. As a result, propagating cracks are tracked automatically through the solution of the phase field PDE, which makes the method very attractive over other numerical approaches that require the explicit or implicit tracking of the discontinuities. Several approaches to phase field modeling of brittle fracture have been independently developed within the physics and mechanics communities, and for a thorough review the reader is encouraged to consult [27]. In the mechanics community, the starting point for deriving the method is the variational formulation of brittle fracture [34], which was regularized in [35], and extended Griffith’s theory of fracture [36].

Despite its many advantages, phase field modeling of brittle fracture has been mostly applied within the context of mesh-based numerical techniques, such as the finite element method (FEM) and isogeometric analysis (IGA) [24–27, 37–39]. Combining particle and meshfree methods with phase field for fracture comes with its own set of challenges, and very few relevant works can be found in the literature [40–48]. To the best of the authors’ knowledge, phase field models of brittle fracture have not been developed and investigated within SPH. In this proof-of-concept paper we develop a phase field model of brittle fracture suitable for SPH, and we demonstrate that phase field is a viable option to model fracture without running into issues that many of the previously used methods exhibit.

This paper is outlined as follows. In Section 2, we review the basics of SPH, with a particular emphasis on total Lagrangian SPH. In Section 3 we provide the basics of phase field modeling of brittle fracture, with a focus on hyperbolic phase field models that are amenable to explicit time integration. In Section 4 we outline the proposed framework for coupling SPH with phase field. Section 5 contains several challenging numerical examples. Section 6 draws conclusions and outlines future research directions.

2. SPH approximation and the Total Lagrangian SPH

2.1. Conventional SPH approximation

The SPH approach was initially proposed as a smoothed interpolation technique to deal with problems related to astrophysics [1, 2]. The fundamental principle of SPH requires the integral representation of functions. The SPH utilizes a weighted interpolation technique to approximate the value of any arbitrary function $f \equiv f(\mathbf{x})$ at any arbitrary point \mathbf{x} in euclidean space. This is also

known as the kernel approximation and can be written as [1, 2]

$$f(\mathbf{x}) \approx \int_{\Omega_{\mathbf{x}}} f(\mathbf{x}') W(r, h) d\mathbf{x}', \quad (1)$$

where $\mathbf{x}' \in \Omega_{\mathbf{x}}$ refers to the spatial coordinates of all the point located within the interpolation space $\Omega_{\mathbf{x}}$ of point \mathbf{x} . The term $W \equiv W(r, h)$, known as the kernel, represents the interpolation weights as a function of the euclidean distance $r = |\mathbf{x} - \mathbf{x}'|$, and the smoothing length $h = 1.33\Delta x$, where Δx is the initial particle spacing. The interpolant in Eq.(1) reproduces the function f exactly if the kernel is a delta function; that is $W = 1$ if $\mathbf{x}' = \mathbf{x}$, and $W = 0$ if $\mathbf{x}' \neq \mathbf{x}$. In practice, the kernel is chosen to be a compactly supported function and approaches the delta function as $h \rightarrow 0$.

The essential advantage of the SPH interpolation is that it allows an exact differentiation of the interpolant to produce the derivatives of function f . The spatial derivatives of f can be computed using the exact differentiation of the kernel as [1, 2]

$$\nabla f \approx \int_{\Omega_{\mathbf{x}}} f(\mathbf{x}') \nabla W d\mathbf{x}'. \quad (2)$$

However, this kind of approximation does not vanish if the function is constant. To improve the accuracy of SPH for constant fields, Eq.(2) is rewritten by replacing f with Φf , allowing for the nabla operator to be written as $\nabla(\Phi f) = \Phi \nabla f + f \nabla \Phi$. Thus, the derivative of the function becomes

$$\nabla f = \frac{1}{\Phi} [\nabla(\Phi f) - f \nabla \Phi], \quad (3)$$

where Φ is any differentiable field. Generally, in continuum mechanics related applications, Φ is set to be the density ρ since it represents a physical quantity in the continuity equation. By doing so, one arrives at the following form of SPH approximation which delivers a zero derivative for constant functions [8]

$$\nabla f(\mathbf{x}) \approx \frac{1}{\rho(\mathbf{x})} \int_{\Omega_{\mathbf{x}}} \rho(\mathbf{x}') [f(\mathbf{x}') - f(\mathbf{x})] \nabla W d\mathbf{x}'. \quad (4)$$

In a spatially discretized SPH particle domain Eq.(1) and Eq.(4) are written as

$$f_i \approx \sum_{j=1}^{N_i} f_j W_{ij} V_j, \quad (5)$$

$$\frac{\partial f_i}{\partial x_i^s} \approx \frac{1}{\rho_i} \sum_{j=1}^{N_i} \rho_j (f_j - f_i) \frac{\partial W_{ij}}{\partial x_j^s} V_j, \quad (6)$$

in which N_i is the total number of particles located within the interpolation space, also known as the neighborhood, influence, or support domain, of particle \mathbf{i} . V_j is the infinitesimal volume of particle \mathbf{j} . W_{ij} is the kernel function relating the particles \mathbf{i} and \mathbf{j} , x_j^s is the s component of the spatial (or Eulerian) coordinate of particle \mathbf{j} , and ρ_j is the density of particle \mathbf{j} .

As noted in [7, 11, 49], the discretization scheme introduced in Eq.(5) and Eq.(6) suffers from the particle inconsistency arising from the non-homogeneous distribution of particles and truncation of the support domain near the boundaries, as seen in Fig. 1. This leads to a lack of conservation of mass, and linear and angular momentum. A number of correction strategies to restore the

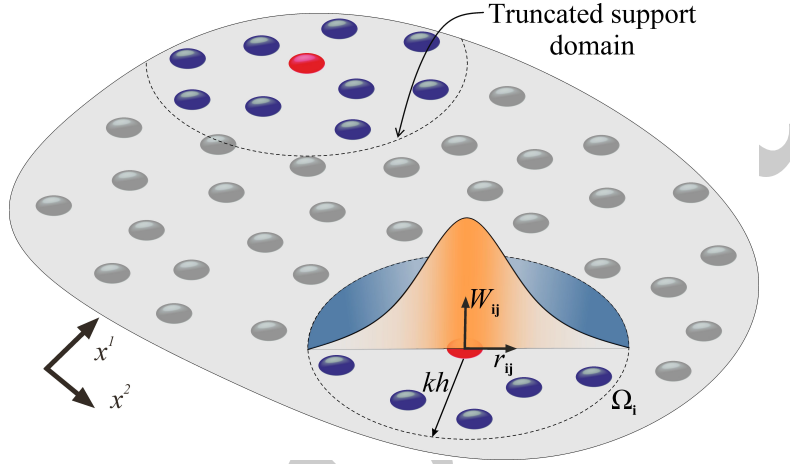


Figure 1: Discretized SPH particle domain with the illustration of full and truncated supports.

particle consistency based on the kernel and gradient correction have been introduced [7, 12, 50]. For its simplicity, throughout this paper, we follow the gradient correction approach presented in [7], in which the gradient is corrected as $\tilde{\nabla} W_{ij} = \mathbf{C}_i \cdot \nabla W_{ij}$.

$$\mathbf{C}_i = - \left(\sum_{j=1}^{N_i} (\nabla W_{ij} \otimes \mathbf{r}_{ij}) V_j \right)^{-1}, \quad (7)$$

is a second rank correction tensor, and $\mathbf{r}_{ij} = \mathbf{x}_i - \mathbf{x}_j$ is the relative position vector of particles \mathbf{i} and \mathbf{j} . The use of \mathbf{C}_i ensures that the gradient of any linear velocity field is exactly evaluated. From this point forward, for brevity, we will omit the approximation sign and will use “ ∇W_{ij} ” or “ $\partial W / \partial \mathbf{x}$ ” to refer to the corrected form of the kernel gradient $\tilde{\nabla} W_{ij} = \mathbf{C}_i \cdot \nabla W_{ij}$.

2.2. SPH in Total Lagrangian form

So far, the general procedure for SPH as an approximation technique was presented. In this section, we further explore its applicability for solid mechanics related applications. It is well established that, when SPH is applied to solve the governing equations of solid mechanics, the

use of Eulerian kernels (kernels defined on Eulerian coordinates) leads to the so-called tensile instability [5, 51]. Such kind of instability is observed in the form of material distortion under tensile stress state. This phenomenon was first noticed in [5] by carrying out the Von Neumann stability analysis (see [5] for detailed explanation). The authors in [5] concluded that for a stable solution the following condition should be satisfied

$$\frac{\partial^2 W}{\partial \mathbf{x}^2} \sigma \leq 0, \quad (8)$$

where σ is the stress. This implies that as long as the left hand side of Eq.(8) is greater than 0 for a particle, the SPH approximation delivers unstable solutions. Several remedies have been suggested to overcome such instability. For example, [52] suggested an approach based on “Mutating the kernel” (see Section 6.6 of [52]). Since the tensile instability has a close relation with the second derivative of the kernel, using a proper kernel will result in a stable solution. However, such an approach is only effective in special cases [9]. Instead, the authors in [6] suggested the use of “stress points” in which additional computational nodes are introduced away from the original SPH particles to carry the stress information separately. However, in [53] it was noted that the use of Eulerian kernels along with the stress points does not fully mitigate the innate instability of SPH. The authors in [53] proposed the use of Lagrangian kernels which deliver a more stable solution. The difference between Eulerian and Lagrangian kernels is that the former is a function of Eulerian (or spatial) coordinates, whereas the later is established based on the Lagrangian/reference (or material) coordinates.

In the Total Lagrangian SPH (TLSPH) formalism, the kernel function and its derivatives are written as functions of the Lagrangian coordinates, thus, leading to the TLSPH approximation of the arbitrary function and its derivative as

$$f_i = \sum_{j=1}^{N_i} \frac{m_{0j}}{\rho_{0j}} f_j W_{0ij}, \quad (9)$$

$$\frac{\partial f_i}{\partial X_i^s} = \frac{1}{\rho_{0i}} \sum_{j=1}^{N_i} m_{0j} (f_j - f_i) \frac{\partial W_{0ij}}{\partial X_j^s}, \quad (10)$$

where

$$\mathbf{X} = \mathbf{x} - \mathbf{u}. \quad (11)$$

W_{0ij} , m_0 , and ρ_0 are the kernel, mass, and density of the associated particle evaluated in the reference (initial) configuration, respectively. \mathbf{u} is the displacement and \mathbf{X} is the Lagrangian coordinate, as depicted in Fig. 2. One major advantage of TLSPH is that, unlike the conventional SPH, its support domain does not change and is evaluated only once at the beginning of the simulation. This

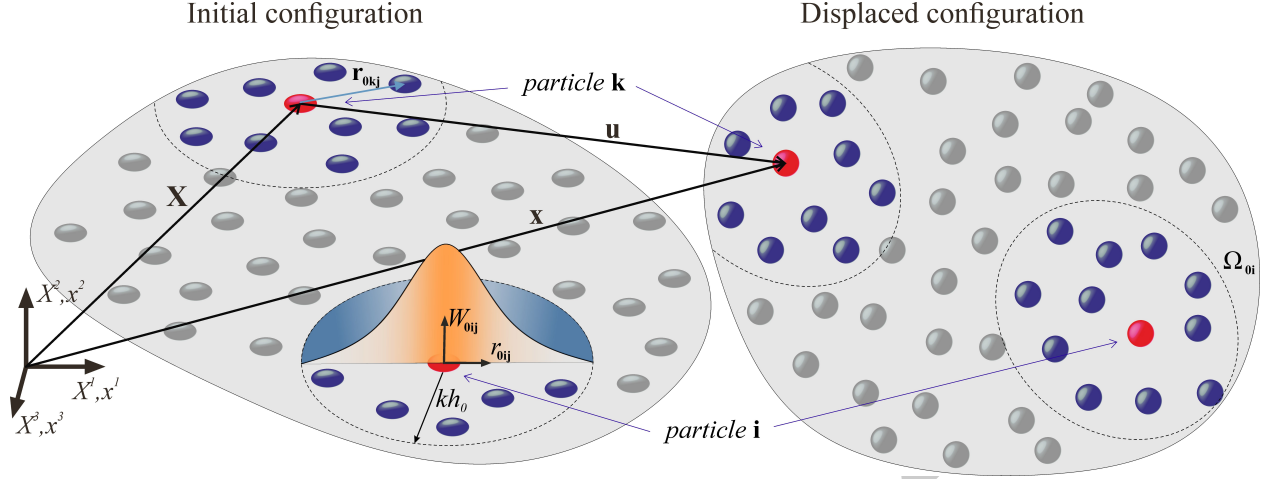


Figure 2: Initial and displaced configuration in TLSPH.

decreases the computational cost considerably. However, it becomes problematic in situations where the domain distortion is such that it leads to significant changes in a particle's neighbors. Cases like this are not considered in this paper and will be studied in subsequent works.

2.3. Governing Equations in TLSPH framework

In this section we present the governing equation of elastic dynamics in TLSPH formalism. Our primary concern is the conservation of momentum, given that the mass is constant and the total energy is naturally conserved. In elastodynamics, the momentum balance equation in the reference configuration is written as [53]

$$\frac{d\mathbf{v}}{dt} = \frac{1}{\rho_0} \nabla_0 \cdot \mathbf{P} + \mathbf{b}_0 \text{ in } \Omega_0, \quad (12)$$

where Ω_0 is the domain of the continuum body in the reference coordinates, and \mathbf{v} , \mathbf{b}_0 , and t , are the velocity, external force, and time, respectively. $\nabla_0 \cdot \mathbf{P}$ is the divergence of the first Piola-Kirchhoff stress tensor with respect to the reference coordinates. The first Piola-Kirchhoff stress tensor, \mathbf{P} , is computed through an appropriate constitutive model, in which the deformation gradient is the corresponding measure of deformation. Details of the specific constitutive models employed in this work will be presented in subsequent sections. The deformation gradient is given as

$$\mathbf{F} = \frac{\partial \mathbf{x}}{\partial \mathbf{X}} = \frac{\partial (\mathbf{u} + \mathbf{X})}{\partial \mathbf{X}} = \frac{\partial \mathbf{u}}{\partial \mathbf{X}} + \mathbf{I}, \quad (13)$$

where \mathbf{I} is the identity matrix. In order to calculate the deformation gradient for particle \mathbf{i} we utilize the TLSPH approach as follows

$$\mathbf{F}_i = \mathbf{I} + \frac{1}{\rho_{0i}} \sum_{j=1}^{N_i} m_{0j} (\mathbf{u}_j - \mathbf{u}_i) \otimes \nabla_0 W_{0ij}, \quad (14)$$

or in index notation as

$$F_i^{ks} = \delta^{ks} + \frac{1}{\rho_{0i}} \sum_{j=1}^{N_i} m_{0j} u_{ji}^k \frac{\partial W_{0ij}}{\partial X_j^s}, \quad (15)$$

in which u_{ji}^k is the k component of the displacement difference vector $\mathbf{u}_{ji} = \mathbf{u}_j - \mathbf{u}_i$, and δ^{ks} is the Kronecker delta. Recall that $\partial W_{0ij}/\partial X_j^s$ is the corrected derivative of the Lagrangian kernel (see Section 2.1). Similarly, Eq.(12) can be written for particle \mathbf{i} as [54]

$$\frac{d\mathbf{v}_i}{dt} = \sum_{j=1}^{N_i} m_{0j} \left(\frac{\mathbf{P}_i}{\rho_{0i}^2} + \frac{\mathbf{P}_j}{\rho_{0j}^2} + \mathbf{P}_{vij} \right) \cdot \nabla_0 W_{0ij} + \mathbf{b}_{0i}, \quad (16)$$

or in index notation as

$$\frac{dv_i^k}{dt} = \sum_{j=1}^{N_i} m_{0j} \left(\frac{P_i^{ks}}{\rho_{0i}^2} + \frac{P_j^{ks}}{\rho_{0j}^2} + P_{vij}^{ks} \right) \frac{\partial W_{0ij}}{\partial X_j^s} + b_{0i}^k, \quad (17)$$

where Einstein's summation rule is employed for the repeated index s . Furthermore, the artificial viscosity term $\mathbf{P}_{vij} = \det(\mathbf{F}_i) \pi_{ij} \mathbf{F}_i^{-1}$ is included to avoid numerical instabilities arising from zero-energy mode discrepancy in the form of a jump in the field variables or shock waves [13, 16, 55, 56]. Following the work of [56] we compute the coefficient π_{ij} as

$$\pi_{ij} = \frac{1}{\rho_{0i}} (\beta_2 \mu_{ij}^2 - \beta_1 c_{0i} \mu_{ij}), \quad (18)$$

in which

$$c_{0i} = c_0 = \sqrt{\frac{\kappa + \frac{4}{3}\mu}{\rho_{0i}}} \quad (19)$$

is the speed of sound at particle \mathbf{i} , $\kappa = E/(3(1 - 2\nu))$ is the bulk modulus, and $\mu = E/(2(\nu + 1))$ is the Lamé parameter, with E and ν being the elastic modulus and Poisson's ratio, respectively. β_1 and β_2 are scalar factors, and μ_{ij} is calculated as

$$\mu_{ij} = \frac{h (\mathbf{v}_i - \mathbf{v}_j) \cdot (\mathbf{X}_i - \mathbf{X}_j)}{r_{0ij}^2 + 0.001h^2}. \quad (20)$$

Here $r_{0ij} = |\mathbf{X}_i - \mathbf{X}_j|$ is the initial distance between particle \mathbf{i} and \mathbf{j} . In most of the numerical examples in this paper we set β_1 and β_2 to 0.04. Note that for larger values of time step and lower particle resolutions higher β_1 and β_2 values may be necessary.

3. Griffith's theory of brittle fracture and the phase field approximation

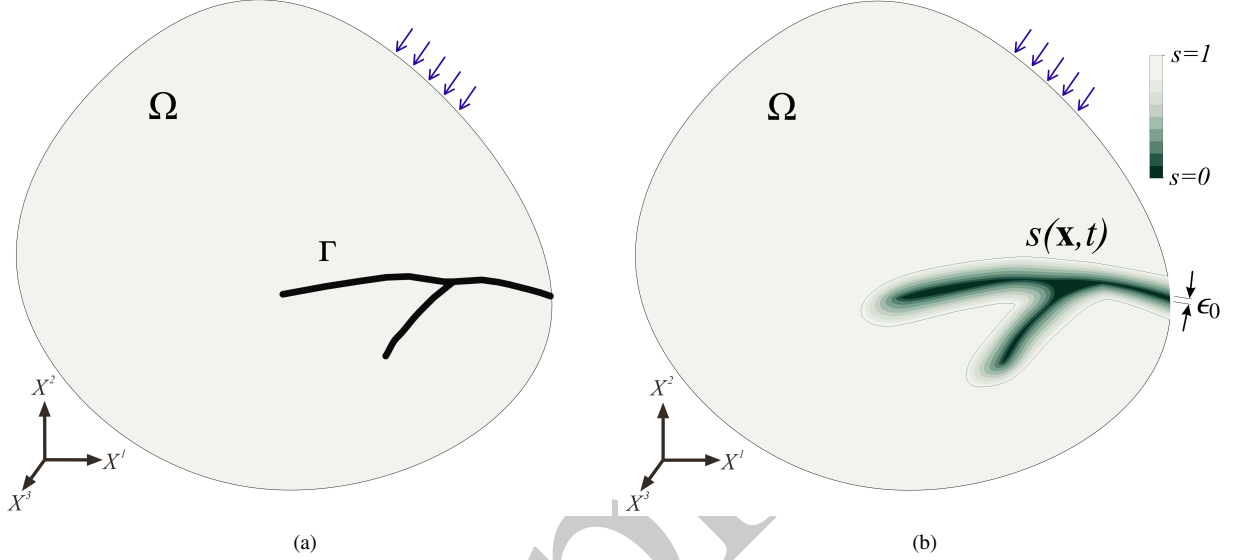


Figure 3: (a) A solid body Ω with internal discontinuity Γ . (b) Approximation of the internal discontinuity by the phase field $s(\mathbf{x}, t)$. ϵ_0 is the length scale parameter that controls the width of the discontinuity.

In this section, to be self contained, we briefly present the basics of phase field modeling of brittle fracture. In the mechanics community, the prevailing models mostly originate from the variational formulation of brittle fracture [34] and the related regularized formulation [27, 35]. According to Griffith's theory of brittle fracture [36], the fracture energy density G_c is the amount of energy required to open a unit area of crack surface. Then, the total potential energy of an elastic body Ω , being the sum of the elastic energy and the fracture energy, is given by the expression

$$\Pi_p(\mathbf{u}, \Gamma) = \int_{\Omega} \psi_e(\boldsymbol{\varepsilon}(\mathbf{u})) d\mathbf{x} + \int_{\Gamma} G_c d\Gamma, \quad (21)$$

where ψ_e is the elastic strain energy density, the details of which will be presented in subsequent sections, $\boldsymbol{\varepsilon}$ is the infinitesimal strain tensor, and Γ is the evolving internal discontinuity boundary which represents a set of discrete cracks. Extending this approach to dynamic problems the kinetic energy is defined as

$$\Pi_k(\dot{\mathbf{u}}) = \frac{1}{2} \int_{\Omega} \rho (\dot{\mathbf{u}} \cdot \dot{\mathbf{u}}) d\mathbf{x}, \quad (22)$$

where ρ is the material density and the superimposed dot denotes time differentiation. Combining the kinetic energy with the potential energy of Eq.(21) we arrive at the Lagrangian of the discrete fracture problem

$$L(\mathbf{u}, \dot{\mathbf{u}}, \Gamma) = \Pi_k(\dot{\mathbf{u}}) - \Pi_p(\mathbf{u}, \Gamma) = \int_{\Omega} \left(\frac{1}{2} \rho (\dot{\mathbf{u}} \cdot \dot{\mathbf{u}}) - \psi_e(\boldsymbol{\varepsilon}(\mathbf{u})) \right) d\mathbf{x} - \int_{\Gamma} G_c d\Gamma. \quad (23)$$

The Euler-Lagrange equations of this functional determine the equations of motion of the body, including the entire process of crack initiation, propagation, and branching of preexisting cracks. However, the numerical treatment is quite complex because tracking the evolving discontinuity Γ is required, which leads to complicated and expensive computations [24, 26]. Therefore, to circumvent the above-mentioned difficulties, the regularized expression for the fracture energy was instead proposed in [35] given as

$$\int_{\Gamma} G_c d\Gamma \approx \int_{\Omega} G_c \left(\frac{(1-s)^2}{4\epsilon_0} + \epsilon_0 |\nabla s|^2 \right) d\mathbf{x}, \quad (24)$$

where s is the so-called phase field parameter (or damage parameter) which represents the fracture surface Γ . It is a continuous variable that describes the smooth transition from the undamaged state ($s = 1$) to the fully damaged one ($s = 0$). ϵ_0 is a parameter that has dimension of a length and controls the width of the smooth approximation of the crack (see Fig. 3). When $\epsilon_0 \rightarrow 0$ the phase field approximation converges to the discrete fracture surface. To model the loss of material stiffness, the elastic strain energy density is defined as [25, 26]

$$\psi_e(\boldsymbol{\varepsilon}, s) = s^2 \psi_e^+ + \psi_e^-. \quad (25)$$

ψ_e^+ and ψ_e^- are the positive and negative elastic strain energy densities, respectively, which will be defined in the next section according to the particular constitutive models employed. As can become evident from Eq.(25), crack propagation is only allowed in tension since the phase field parameter is applied only to the tensile part of the elastic strain energy. By substituting the phase field approximations for the fracture energy Eq.(24) and the elastic energy density Eq.(25) into the expression for the Lagrangian functional Eq.(23), and by deriving the corresponding Euler-Lagrange equations, we arrive at the strong form equations of motion that consist of the momentum balance presented in Eq.(12) and the phase field parameter evolution equation

$$\left(\frac{4\epsilon_0 \psi_e^+}{G_c} + 1 \right) s - 4\epsilon_0^2 \nabla^2 s = 1 \text{ in } \Omega_0, \quad (26)$$

where $\nabla^2 s$ is the Laplacian of s .

Remark 1. It can be seen that the kinetic energy term in the Lagrange energy functional is not affected by the phase field parameter s , which leads to conservation of mass.

In order to model the irreversibility condition (cracks do not heal) a history functional is introduced as

$$\mathcal{H}(\mathbf{X}, t) = \max_{\tau \leq t} (\psi_e^+(\mathbf{X}, \tau)), \quad (27)$$

and is used in place of the tensile elastic strain energy ψ_e^+ in the phase field's governing equation. The updated strong form that governs the evolution of the phase field parameter is

$$\left(\frac{4\epsilon_0 \mathcal{H}}{G_c} + 1 \right) s - 4\epsilon_0^2 \nabla^2 s = 1 \text{ in } \Omega_0. \quad (28)$$

Finally, initial conditions need to be introduced for the history functional, i.e.

$$\mathcal{H}(\mathbf{X}, 0) = \mathcal{H}_0(\mathbf{X}). \quad (29)$$

The initial condition of the history functional $\mathcal{H}_0(\mathbf{X})$ can be used to model preexisting cracks in the domain. Eq.(28) and the corresponding initial condition Eq.(29) need to be solved together with the equations of motion (e.g. momentum balance Eq.(12)) to compute both the displacement field $\mathbf{u}(\mathbf{X}, t)$ and the phase field parameter $s(\mathbf{X}, t)$.

Although the aforementioned approach and its variants have been successfully applied within the context of numerical methods based on implicit time integration, they become problematic when lumped-mass explicit dynamics schemes are employed. The reason is that Eq.(28) is an elliptic PDE, and therefore a linear system needs to be solved in every time step to determine the phase field parameter. Though it is possible from an implementation point of view, the solution of an elliptic equation in every explicit step would make the approach computationally expensive. To overcome this difficulty, phase field models which include time dependency have been proposed. In [24] the phase field parameter evolves according to a parabolic PDE as

$$\frac{1}{M} \dot{s} + 2s\psi_e^+ - G_c \left(2\epsilon_0 \nabla^2 s + \frac{1-s}{2\epsilon_0} \right) = 0 \text{ in } \Omega_0, \quad (30)$$

where M is a parameter controlling the rate at which local damage information diffuses into the bulk material. Clearly, when $M \rightarrow \infty$ the model approaches the standard elliptic models like the one of Eq.(26). However, Eq.(30) is a heat-equation-like PDE, and is subjected to an unfavorable CFL condition when explicit time integration is employed [57]

$$\Delta t \leq \Delta x^2, \quad (31)$$

where Δt and Δx are time and length scales associated with the discretization. Therefore, the authors in [57] proposed a novel model in which the phase field parameter evolves according to a hyperbolic PDE by adding a second-order time derivative to the model of Eq.(30). The resulting PDE is

$$\frac{2G_c\epsilon_0}{c^2}\ddot{s} + \frac{1}{M}\dot{s} + 2s\psi_e^+ - G_c\left(2\epsilon_0\nabla^2s + \frac{1-s}{2\epsilon_0}\right) = 0 \text{ in } \Omega_0. \quad (32)$$

c is a speed limit on the propagation of the phase field parameter through the undamaged material and is taken to be equal to the sound speed given in Eq.(19). The model of Eq.(32) is subjected to the hyperbolic stability condition of

$$c\Delta t \leq \Delta x, \quad (33)$$

which is much less restrictive than the parabolic one (Eq.(31)), especially in the limit of $\Delta x \rightarrow 0$. To avoid any wave-like behavior due to the hyperbolic nature of the governing equation, the authors in [57] proposed an upper bound on M such that the system is overdamped and the behavior of the phase field parameter is monotonic. The upper bound is given as

$$M < \frac{c}{2\sqrt{4G_c\epsilon_0\psi_e + G_c^2}}. \quad (34)$$

Finally, the irreversibility condition is enforced in a way similar to the elliptic problem (Eq.(27)) and the updated hyperbolic governing equation for the phase field damage parameter becomes

$$\frac{2G_c\epsilon_0}{c^2}\ddot{s} + \frac{1}{M}\dot{s} + 2s\mathcal{H} - G_c\left(2\epsilon_0\nabla^2s + \frac{1-s}{2\epsilon_0}\right) = 0 \text{ in } \Omega_0, \quad (35)$$

with the initial condition of Eq.(29), whereas the upper bound on the parameter M becomes

$$M < \frac{c}{2\sqrt{4G_c\epsilon_0\mathcal{H} + G_c^2}}. \quad (36)$$

Since SPH is traditionally an explicit method, the hyperbolic version of the phase field PDE (Eq.(35)) is employed in this work.

4. The TLSPH-Phase field approach

4.1. Governing equations

With the two previous sections at hand (Section 2 and Section 3), we present a total Lagrangian SPH framework for the solution of the coupled elastodynamics–phase field problem expressed

through the following strong form governing equations of motion,

$$(S) \begin{cases} \frac{d\mathbf{v}}{dt} = \frac{1}{\rho_0} \nabla_0 \cdot \mathbf{P} + \mathbf{b}_0 & \text{in } \Omega_0 \\ \frac{2G_c \epsilon_0}{c^2} \ddot{s} + \frac{1}{M} \dot{s} + 2s\mathcal{H} - G_c \left(2\epsilon_0 \nabla^2 s + \frac{1-s}{2\epsilon_0} \right) = 0 & \text{in } \Omega_0 \end{cases} . \quad (37)$$

In the above-mentioned coupled problem, the first equation corresponds to the balance of linear momentum, that was briefly outlined in Section 2, whereas the second equation corresponds to the phase field (damage) parameter evolution. The solution of the phase field PDE is based upon the basics of TLSPH, and the overall solution procedure is outlined in this section. Before proceeding to the solution procedure we provide the details of the constitutive model.

4.2. Constitutive modeling

In Section 2 we presented the basics of TLSPH in terms of the first Piola-Kirchhoff stress, whereas in Section 3 we outlined the basics of the phase field approach for brittle fracture in terms of a general elastic strain energy density ψ_e . Here, we provide the details of the elastic strain energy density and the corresponding constitutive equations based on two hyperelastic models; the isotropic Saint-Venant Kirchhoff and the neo-Hookean model. However, we would like to point out that other constitutive models can be used with the proposed framework.

4.2.1. Saint-Venant Kirchhoff

The Saint-Venant Kirchhoff model can be easily derived by extending the linear-elastic framework presented in [26] to large rotations. This is achieved by replacing the infinitesimal strain tensor with the Green-Lagrange strain tensor $\mathbf{E} = \frac{1}{2}(\mathbf{F}^T \mathbf{F} - \mathbf{I})$. Then, the elastic strain energy density functional becomes

$$\psi_e = \frac{1}{2} \lambda (\text{tr} \mathbf{E})^2 + \mu \text{tr}(\mathbf{E}^2), \quad (38)$$

where $\lambda = \kappa - \frac{2}{3}\mu$ and $\mu = E/(2(\nu + 1))$ are the Lamé parameters. We then define

$$\psi_e^+ = \frac{1}{2} \lambda \{\text{tr} \mathbf{E}\}_+^2 + \mu \text{tr}(\mathbf{E}^+ \mathbf{E}^+), \quad (39)$$

$$\psi_e^- = \frac{1}{2} \lambda \{\text{tr} \mathbf{E}\}_-^2 + \mu \text{tr}(\mathbf{E}^- \mathbf{E}^-), \quad (40)$$

where the following decomposition is employed

$$\mathbf{E}^+ = \mathbf{Q} \mathbf{\Lambda}^+ \mathbf{Q}^T, \quad (41)$$

$$\mathbf{E}^- = \mathbf{Q} \mathbf{\Lambda}^- \mathbf{Q}^T, \quad (42)$$

$$\mathbf{E} = \mathbf{Q} \mathbf{\Lambda} \mathbf{Q}^T. \quad (43)$$

$\Lambda = \text{diag}(\lambda_1, \lambda_2, \lambda_3)$ has the eigenvalues of \mathbf{E} on its diagonal, \mathbf{Q} has the corresponding eigenvectors as its columns, $\Lambda^\pm = \text{diag}(\lambda_1^\pm, \lambda_2^\pm, \lambda_3^\pm)$, and $\{\cdot\}_\pm$ selects the \pm part of its argument, i.e.

$$\{x\}_\pm = \begin{cases} x & x \in \mathbb{R}^\pm \\ 0 & \text{otherwise} \end{cases}. \quad (44)$$

The second Piola–Kirchhoff stress can then be computed by differentiating the strain energy density ψ_e with respect to the Green-Lagrange strain tensor \mathbf{E} ,

$$\mathbf{S}^\pm = \frac{\partial \psi_e^\pm}{\partial \mathbf{E}} = \lambda \{\text{tr} \mathbf{E}\}_\pm \mathbf{I} + 2\mu \mathbf{E}^\pm, \quad (45)$$

and

$$\mathbf{S} = s^2 \mathbf{S}^+ + \mathbf{S}^-. \quad (46)$$

Finally, the first Piola–Kirchhoff stress can be computed as

$$\mathbf{P} = \mathbf{F} \mathbf{S}. \quad (47)$$

4.2.2. Neo-Hookean

The Saint-Venant Kirchhoff model is known to exhibit instabilities in the case of strong compression [58]. Thus, for the problems in this paper involving strong compression, we employ a Neo-Hookean material. For the Neo-Hookean model we follow the presentation in [42, 59]. The positive and negative parts of the elastic strain energy density are given as

$$\psi_e^+ = \begin{cases} U(J) + \bar{\psi}_e(\bar{\mathbf{b}}) & J \geq 1 \\ \bar{\psi}_e(\bar{\mathbf{b}}) & J < 1, \end{cases} \quad (48)$$

$$\psi_e^- = \begin{cases} 0 & J \geq 1 \\ U(J) & J < 1, \end{cases} \quad (49)$$

where

$$U(J) = \frac{1}{2} \kappa \left(\frac{1}{2} (J^2 - 1) - \ln J \right), \quad (50)$$

$$\bar{\psi}_e(\bar{\mathbf{b}}) = \frac{1}{2} \mu (\text{tr} \bar{\mathbf{b}} - 3), \quad (51)$$

$$J = \det \mathbf{F}, \quad (52)$$

$$\mathbf{b} = \mathbf{F} \mathbf{F}^T, \quad (53)$$

$$\bar{\mathbf{b}} = J^{-2/3} \mathbf{b}. \quad (54)$$

The second Piola–Kirchhoff stress can then be computed as

$$\mathbf{S} = 2 \frac{\partial \psi_e}{\partial \mathbf{b}}. \quad (55)$$

For the given elastic strain energy density this results in

$$\mathbf{S} = 2 \begin{cases} s^2 \left(U'(J) \frac{\partial J}{\partial \mathbf{b}} + \frac{\partial \bar{\psi}_e(\bar{\mathbf{b}})}{\partial \bar{\mathbf{b}}} \right) & J \geq 1 \\ U'(J) \frac{\partial J}{\partial \mathbf{b}} + s^2 \frac{\partial \bar{\psi}_e(\bar{\mathbf{b}})}{\partial \bar{\mathbf{b}}} & J < 1. \end{cases} \quad (56)$$

The derivatives in the above expression are computed as

$$U'(J) = \frac{1}{2} \kappa (J - J^{-1}), \quad (57)$$

$$\frac{\partial J}{\partial \mathbf{b}} = \frac{\partial \sqrt{\det \mathbf{b}}}{\partial \mathbf{b}} = \frac{1}{2} J \mathbf{b}^{-1}, \quad (58)$$

$$\frac{\partial \bar{\psi}_e}{\partial \mathbf{b}} = \frac{\partial \bar{\psi}_e}{\partial \bar{\mathbf{b}}} \frac{\partial \bar{\mathbf{b}}}{\partial \mathbf{b}} = \frac{J^{-2/3}}{2} \mu \left(\mathbf{I} - \frac{1}{3} (\text{tr} \mathbf{b}) \mathbf{b}^{-1} \right). \quad (59)$$

Substituting the above equations into Eq.(56) we get

$$\mathbf{S} = \begin{cases} s^2 \left(\frac{1}{2} \kappa (J^2 - 1) \mathbf{b}^{-1} + J^{-2/3} \mu \left(\mathbf{I} - \frac{1}{3} (\text{tr} \mathbf{b}) \mathbf{b}^{-1} \right) \right) & J \geq 1 \\ \frac{1}{2} \kappa (J^2 - 1) \mathbf{b}^{-1} + s^2 \left(J^{-2/3} \mu \left(\mathbf{I} - \frac{1}{3} (\text{tr} \mathbf{b}) \mathbf{b}^{-1} \right) \right) & J < 1. \end{cases} \quad (60)$$

Finally, the first Piola–Kirchhoff stress is computed as in Eq.(47).

4.3. Solution procedure and numerical implementation

We first define two common terms that will be used regularly throughout this paper, the soft particle and the phase field limit.

Definition 1. Soft (damaged) particle refers to any SPH particle whose phase field parameter drops sufficiently so that its stress is fairly low, and thus the effect on neighboring particles is negligible. From a numerical implementation point of view, soft particles behave as rigid objects having inertia but no internal force.

Definition 2. The phase field limit refers to the threshold value of the phase field parameter below which the particle is assumed to be a soft particle.

In order to compute the first Piola–Kirchhoff stress through the constitutive model presented in

the previous subsection, we redefine the deformation gradient as

$$\mathbf{F}_i = \begin{cases} \frac{\partial \mathbf{u}_i}{\partial \mathbf{X}_i} + \mathbf{I} & s_i > s_l \\ \mathbf{I} & \text{otherwise} \end{cases}. \quad (61)$$

Here s_l is the phase field limit that determines the particle's stiffness state and $\partial \mathbf{u}_i / \partial \mathbf{X}_i$ is calculated utilizing the corrected form of the TLSPH approach (see Section 2.3) as

$$\frac{\partial u_i^k}{\partial X_i^s} = \frac{1}{\rho_{0i}} \sum_{j=1}^N m_{0j} u_{ji}^k \frac{\partial W_{0ij}}{\partial X_j^s}, \quad (62)$$

where u_{ji}^k is the k component of the displacement difference vector $\mathbf{u}_{ji} = \mathbf{u}_j - \mathbf{u}_i$ between particles \mathbf{i} and \mathbf{j} . The kernel function in Eq.(62), and in any other calculation involving SPH interpolation, is chosen to be a cubic spline [60] defined in reference coordinates as

$$W_{0ij} = \begin{cases} 0 & q > 2 \\ \frac{1}{4}C (2 - q)^3 & 1 \leq q \leq 2 \\ C (1 - 1.5q^2 + 0.75q^3) & 0 \leq q \leq 1 \end{cases}, \quad (63)$$

in which $q = |\mathbf{X}_i - \mathbf{X}_j|/h$ and C is a constant determined as

$$C = \begin{cases} 2/(3h) & \text{for one dimensional space} \\ 10/(7\pi h^2) & \text{for two dimensional space} \\ 1/(\pi h^3) & \text{for three dimensional space} \end{cases}, \quad (64)$$

where h is the smoothing length. We further rearrange Eq.(35) as

$$\ddot{s} = \frac{c^2}{2G_c \epsilon_0} \left[G_c \left(2\epsilon_0 \nabla^2 s + \frac{1-s}{2\epsilon_0} \right) - \frac{1}{M} \dot{s} - 2s\mathcal{H} \right] \quad (65)$$

in order to have an explicit definition of the phase field inertia \ddot{s} , in terms of the phase field parameter s , its time derivative \dot{s} , and its Laplacian $\nabla^2 s$. The Laplacian of the phase field is calculated utilizing the SPH Laplacian operator [61] in TLSPH formalism as

$$\nabla^2 s_i = 2 \sum_{j=1}^N (s_i - s_j) V_{0j} \frac{r_{0ij}^s}{|\mathbf{r}_{0ij}|^2} \frac{\partial W_{0ij}}{\partial X_j^s}, \quad (66)$$

where V_{0j} is the initial volume of \mathbf{j} , $|\mathbf{r}_{0ij}|$ is the magnitude of the relative initial position vector $\mathbf{r}_{0ij} = \mathbf{X}_i - \mathbf{X}_j$, and r_{0ij}^s is the s -component of \mathbf{r}_{0ij} . Note that Einstein summation is used for the repeated index s . After solving for the phase field inertia, the phase field and its first time derivative

are evolved explicitly, and the results are used in updating the first Piola-Kirchhoff stress through the corresponding constitutive model. Finally, the momentum balance equation is solved for the other TLSPH field variables, e. g. \mathbf{v} , $\dot{\mathbf{v}}$, \mathbf{u} .

Remark 2. It can be observed that for soft particles ($s_i < s_l$) the deformation is assumed to be zero (Eq.(61)). Although in reality soft particles have obviously non-zero deformations, this is a convenient assumption that improves the numerical stability of the proposed algorithm, and does not affect the physics of the problem since the deformation gradient is only used in the stress computation which is close to zero for soft particles. From a numerical implementation perspective, soft particles stick to their neighboring undamaged particles and move with them as rigid bodies, with their only effect to the problem being through means of inertia.

The overall computational procedure of TLSPH-Phase field consists of two main modules; a pre-processing module and a time integration module. In the pre-processing module, the domain is first discretized into particles, the field variables are initialized, and any preexisting discontinuities are introduced. Then, a neighbor search is performed to determine the support domain of each particle. At this stage the conventional kernel and its derivatives are computed using Eq.(63), and then the gradient correction tensor for each particle is computed from Eq.(7). The corrected kernel gradients are subsequently computed and substituted utilizing the $\tilde{\nabla}W_{ij} = \mathbf{C}_i \cdot \nabla W_{ij}$ relation (see Section 2.1). The details of the preprocessing module are given in Algorithm 1.

Remark 3. Traditionally, in phase field for fracture, a preexisting crack is modeled either through a geometrical notch of finite width, or a prescribed value in the history functional, \mathcal{H}_0 . Although both approaches have been extensively and successfully applied in the phase field literature, problems can potentially arise, especially in the case where the discontinuity is introduced as a physical notch. For example, in the case of meshfree and particle methods, care must be taken so that the physical discontinuity is large enough and the supports of the particles in either side of the crack do not overlap. Here, we propose a third way of modeling preexisting cracks, in which the neighbor search for particles that lie in either side of the discontinuity is restricted in that side of the crack only, as can be seen in Fig. 4d. Simply put, we are blocking any communication among particles that lie in different sides of the preexisting crack surface Γ_0 . This way the preexisting discontinuity is modeled easily and exactly without the need for a physical geometrical gap. One major advantage of this approach is that for arbitrarily shaped complex discontinuities a neighbor search restriction can be easily performed, whereas introducing geometrical gaps is fairly complicated. In this paper, we used either the physical gap or the neighbor search restriction approach and observed that both lead to similar results.

When it comes to time integration, a second-order Euler predictor-corrector time integration scheme is adopted with a CFL condition of

Algorithm 1 Preprocessing module for TLSPH-Phase field modeling of brittle fracture

Preprocess

- ▷ Get input from file or user interface
- ▷ Discretize the continuous domain into discrete particles
- ▷ Introduce preexisting discontinuities

for $i \leftarrow 1$ **to** Total number of particles **do**

- ▷ Search for \mathbf{j} neighbor of particle \mathbf{i} in its support domain. Add \mathbf{j} to the neighbor list of \mathbf{i} .
- ▷ Compute kernel W_{0ij} , and its gradient $\nabla_0 W_{0ij}$, between particles \mathbf{i} and \mathbf{j} using Eq.(63).

end for

for $i \leftarrow 1$ **to** Total number of particles **do**

- ▷ Compute gradient correction tensor of particle \mathbf{i} , \mathbf{C}_i , using Eq.(7) or in index form as

$$C_i^{ks} = - \left(\sum_{j=1}^{N_i} r_{0ij}^s \frac{\partial W_{0ij}}{\partial X_j^k} V_{0j} \right)^{-1}, \text{ where } N_i \text{ is the number of neighbours of particle } \mathbf{i}.$$

end for

for $i \leftarrow 1$ **to** Total number of particles **do**

for $j \leftarrow 1$ **to** N_i **do**

- ▷ Correct the kernel gradient as $\frac{\partial W_{0ij}}{\partial X_j^k} = C_i^{ks} \frac{\partial W_{0ij}}{\partial X_j^s}$ (summation is done over index s)

end for

end for

- ▷ Initialize field variables
 - ▷ Apply static loads (if exist)
-

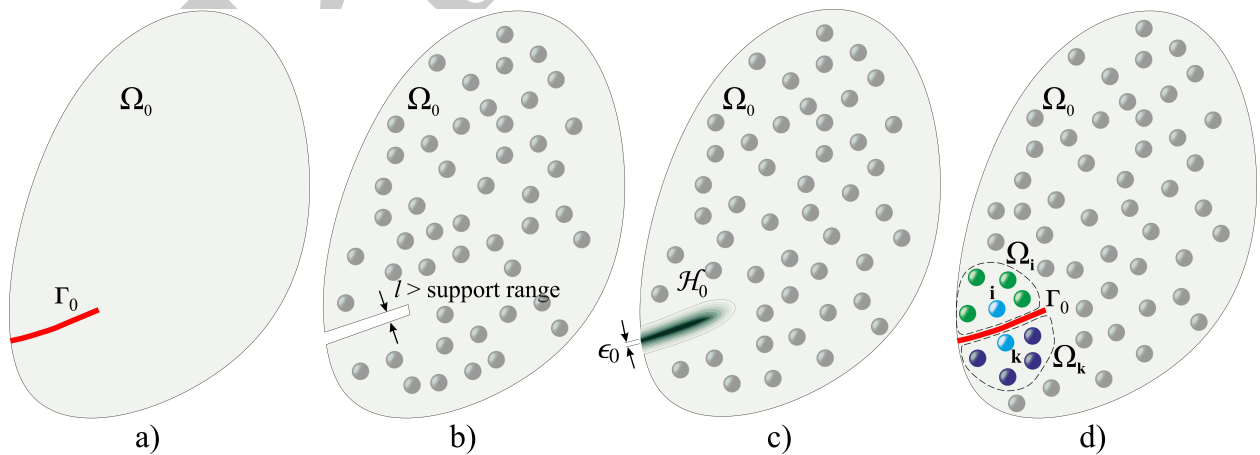


Figure 4: A description of a) preexisting discontinuity and its approximation by means of b) introducing a geometrical notch, c) assigning a prescribed value in the history functional, and d) restricting the neighbor search only among particles that lie in the same side of the discontinuity with the particle under consideration.

$$\Delta t \leq \min \left(0.25 \frac{h}{c_0 + |\mathbf{v}_{max}|}, \frac{\Delta x}{c_0} \right), \quad (67)$$

where the second term ensures the stability of the phase field solution, and \mathbf{v}_{max} is the maximum possible velocity of the computational domain in space and time. At the beginning of each time step the field variables are updated utilizing the predictor scheme as

$$\mathbf{v}_i^{(t+1/2)} = \mathbf{v}_i^{(t)} + 0.5\Delta t \left(\frac{d\mathbf{v}_i}{dt} \right)^{(t-1/2)}, \quad (68)$$

$$\mathbf{u}_i^{(t+1/2)} = \mathbf{u}_i^{(t)} + 0.5\Delta t \mathbf{v}_i^{(t+1/2)}, \quad (69)$$

$$\dot{s}_i^{(t+1/2)} = \dot{s}_i^{(t)} + 0.5\Delta t \ddot{s}_i^{(t-1/2)}, \quad (70)$$

$$s_i^{(t+1/2)} = s_i^{(t)} + 0.5\Delta t \dot{s}_i^{(t+1/2)}, \quad (71)$$

where the superscripts $(t + 1/2)$, $(t - 1/2)$, and (t) denote the values of the related field variable at half time step, previous half time step, and previous time step, respectively. Then, using the values of $\mathbf{u}^{(t+1/2)}$, the deformation gradient of the TLSPH particles is computed using Eqs.(61-62). At this stage, an appropriate constitutive model is utilized (see e.g. Section 4.2.1 or Section 4.2.2) to compute the first Piola-Kirchhoff stress tensor as a function of the computed deformation gradient and the predicted half time step values of phase field (damage). Then, Eq.(17), Eq.(66), and Eq.(65) are in turn solved using the values of the variables at half-time step to compute the acceleration $(d\mathbf{v}/dt)^{(t+1/2)}$, Laplacian of the phase field $(\nabla^2 s)^{(t+1/2)}$, and the phase field inertia $\ddot{s}^{(t+1/2)}$, respectively. Finally, the corrected values for the field variables are computed as

$$\mathbf{v}_i^{(t+1)} = \mathbf{v}_i^{(t)} + \Delta t \left(\frac{d\mathbf{v}_i}{dt} \right)^{(t+1/2)}, \quad (72)$$

$$\mathbf{u}_i^{(t+1)} = \mathbf{u}_i^{(t)} + \Delta t \mathbf{v}_i^{(t+1/2)}, \quad (73)$$

$$\dot{s}_i^{(t+1)} = \dot{s}_i^{(t)} + \Delta t \ddot{s}_i^{(t+1/2)}, \quad (74)$$

$$s_i^{(t+1)} = s_i^{(t)} + \Delta t \dot{s}_i^{(t+1)}, \quad (75)$$

where the $(t + 1)$ superscript denotes the current time step. Algorithm 2 and Algorithm 3 present the implementation of the time integration module and the constitutive models for a single step calculation. It should be noted that for problems involving the contact of two separate bodies an additional interface force is included in the momentum equation (Eq.(17)). Hence, the momentum equation becomes

Algorithm 2 Single step calculations of time integration module for TLSPH-Phase field modeling of brittle fracture

Time integration

▷ Apply dynamic force and/or displacement boundary conditions

for $i \leftarrow 1$ **to** *Total number of particles* **do**

▷ Compute half-time step values of field variables using Eqs.(68-71)

end for

for $i \leftarrow 1$ **to** *Total number of particles* **do**

▷ Compute deformation gradient \mathbf{F}_i as in Eq.(61), using half step displacement values

▷ Utilize Algorithm 3 to calculate \mathbf{P}_i , ψ_{ei}^+ , and ψ_{ei}^- using the appropriate constitutive model

if $\psi_{ei}^+ > \mathcal{H}_i$ **then**

▷ $\mathcal{H}_i = \psi_{ei}^+$ (here we update the history functional)

end if

▷ Compute M_i parameter as in Eq.(36)

▷ Using half-step values of the phase field parameter $s^{(t+1/2)}$ compute the Laplacian $\nabla^2 s_i$ as in Eq.(66)

▷ Using half step values of $s^{(t+1/2)}$ and $\dot{s}^{(t+1/2)}$ compute $\ddot{s}^{(t+1/2)}$ as in Eq.(65)

▷ If contact exists, using half-step values of $\mathbf{x}^{(t+1/2)}$, compute contact force for particle i as in [Appendix A](#)

end for

for $i \leftarrow 1$ **to** *Total number of particles* **do**

▷ Using half step values of field variables compute acceleration $(d\mathbf{v}_i/dt)^{(t+1/2)}$ as in Eq.(17) (or Eq.(76) for problems involving contact interactions)

▷ Correct field variables using Eqs.(72-75)

end for

▷ Write results (occasionally)

Algorithm 3 Implementation of the Saint-Venant Kirchhoff and neo-Hookean hyperelastic constitutive models

If constitutive model is Saint-Venant Kirchhoff:

- ▷ Compute Green-Lagrange strain tensor as $E_i^{ks} = \frac{1}{2} (F_i^{mk} F_i^{ms} + \delta^{ks})$ (summation is done over index m)
- ▷ Decompose \mathbf{E}_i into \mathbf{E}_i^+ and \mathbf{E}_i^- using Eqs.(41-42)
- ▷ Compute ψ_{ei}^+ and ψ_{ei}^- using Eqs.(39-40)
- ▷ Compute \mathbf{S}_i^+ and \mathbf{S}_i^- using Eq.(45)
- ▷ Compute $\mathbf{S}_i = (s_i^{(t+1/2)})^2 \mathbf{S}_i^+ + \mathbf{S}_i^-$
- ▷ Compute $P_i^{ks} = F_i^{km} S_i^{ms}$ (summation is done over index m)

Else if constitutive model is neo-Hookean:

- ▷ Compute J , \mathbf{b} , and $\bar{\mathbf{b}}$ using Eq.(52), Eq.(53), and Eq.(54), respectively.
- ▷ Compute $U(J)$ and $\bar{\psi}_e(\bar{\mathbf{b}})$ using Eq.(50) and Eq.(51), respectively.
- ▷ Compute ψ_{ei}^+ and ψ_{ei}^- using Eq.(48) and Eq.(49), respectively.
- ▷ Compute \mathbf{S}_i from Eq.(60) using half-step values of phase field, $s_i^{(t+1/2)}$.
- ▷ Compute $P_i^{ks} = F_i^{km} S_i^{ms}$ (summation is done over index m)

Else:

- ▷ Apply a different constitutive model here to calculate \mathbf{P}_i , ψ_{ei}^+ , and ψ_{ei}^-
-

$$\frac{dv_i^k}{dt} = \sum_{j=1}^{N_i} m_{0j} \left(\frac{P_i^{ks}}{\rho_{0i}^2} + \frac{P_j^{ks}}{\rho_{0j}^2} + P_{vij}^{ks} \right) \frac{\partial W_{0ij}}{\partial X_j^s} + b_{0i}^k + \sum_{a=1}^{\hat{N}_i} f_{ai} r_{ai}^k \quad (76)$$

where \hat{N}_i is the total number of particles located at a separate body withing the contact distance, r_0 , of particle \mathbf{i} , r_{ai}^k is the k component of the relative position vector $\mathbf{r}_{ai} = \mathbf{x}_a - \mathbf{x}_i$ between particles \mathbf{a} and \mathbf{i} calculated using the eulerian coordinates \mathbf{x} , as given in Fig. 5, and f_{ai} is a scalar multiplier whose details are given in [Appendix A](#). For the cases involving contact interaction in this paper we set $r_0 = 2.5\Delta x$ unless stated otherwise.

5. Numerical examples

In this section, we first apply the proposed TLSPH-Phase field framework to model various challenging problems from the literature. We then illustrate further capabilities of our model by addressing the failure occurrences in a three dimensional contact problem. A CPU parallel code was developed and the simulations were carried out on a 40-core node on SeaWulf cluster located at the Institute for Advanced Computational Science (IACS) at Stony Brook University. The animated videos of the simulations are provided in Electronic Annex I ([Appendix B](#)).

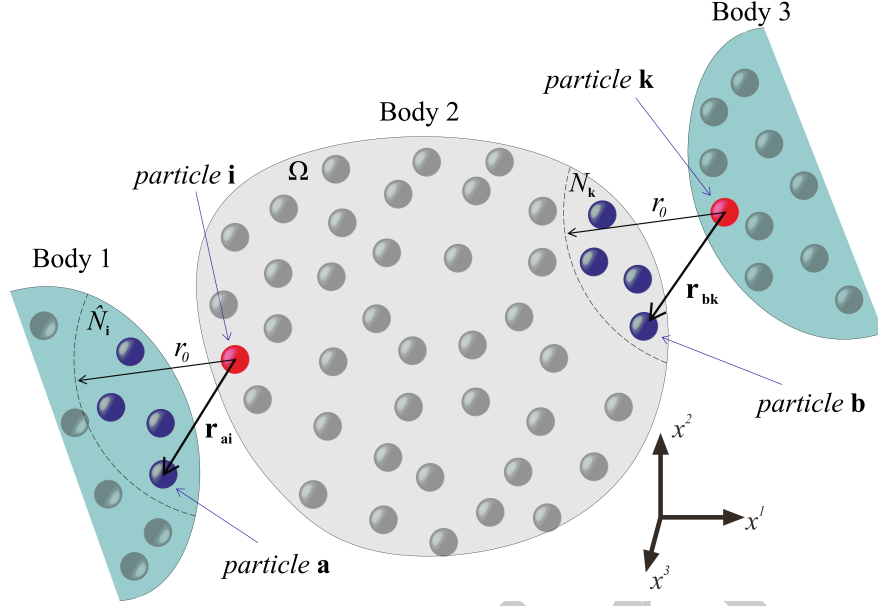


Figure 5: Interface details of the contact domain with multiple body contacts in SPH.

5.1. Symmetric three point bending test

We first solve the crack propagation in a plate subjected to a symmetric three point bending [25, 27]. The length, width, and thickness of the plate, are set to $L_x = 8.2$ mm, $L_y = 2$ mm, and $L_z = \Delta x$, respectively [25, 27]. The material parameters $\lambda = 12$ GPa, $\mu = 8$ GPa, density $\rho_0 = 1190$ kg/m³, and $G_c = 0.54$ kJ/m² are adopted from [25]. The contact parameters, length scale, and time step values, are set to $K_p = 9 \times 10^{12}$ and $r_0 = 2.5\Delta x$, $\epsilon_0 = \Delta x$, and $\Delta t = 0.1$ ns, respectively. A preexisting crack with a length of 0.4 mm is located at the lower central portion of the plate and is modeled by restricting the neighbour search of the particles around the discontinuity region, as suggested in Section 4.3 and Fig. 4d. We enforce the boundary conditions through contact with rigid circular bands with outer diameters of 0.4 mm at three regions, as shown in Fig. 6. The contact force is applied in the X^2 -direction only, and a velocity of -5 m/s in the X^2 -direction is assigned to the upper band, whereas the two lower bands are fixed in the X^1 - and X^2 -directions. We set the artificial viscosity parameters (see Section 2.3) to $\beta_1 = 0.2$ and $\beta_2 = 0$, and a phase field limit of $s_l = 0.1$ is chosen for soft particles. The domain is discretized into 423,665 particles with a particle spacing of $\Delta x = 6.25$ μ m, out of which 3,825 particles belong to the contact bodies. Both the Saint-Venant Kirchhoff and Neo-Hookean constitutive models are employed. Fig. 7 shows the snapshots of the phase field parameter at different stages of the propagation. As can be seen, the propagation starts from the preexisting crack tip, continues in the vertical direction, and stops near the upper boundary of the plate. The start and end time of the propagation correspond to a displacement of 0.045 mm and 0.1 mm of Point A (see Fig. 6)

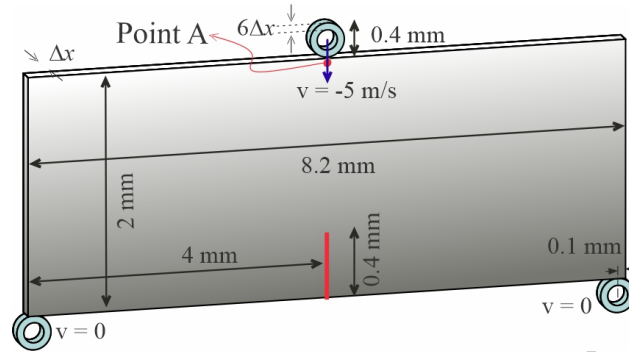


Figure 6: Symmetric three point bending test. Geometry and loading conditions.

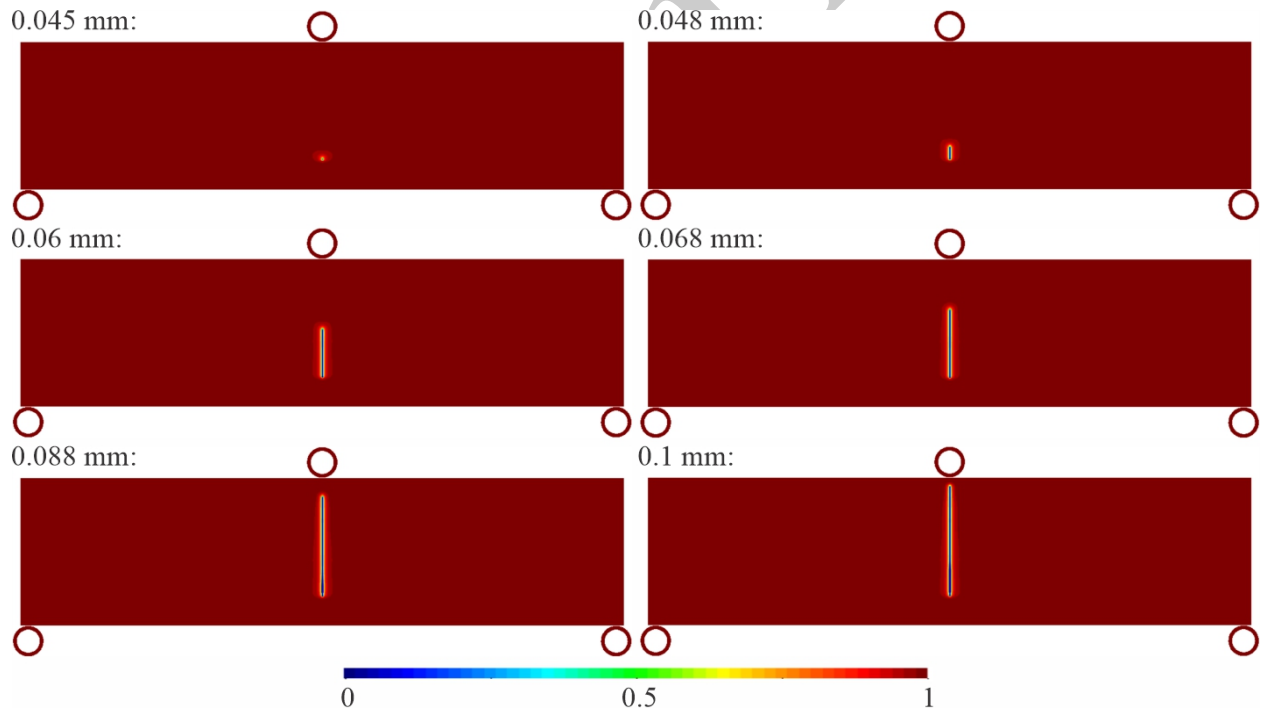


Figure 7: Symmetric three point bending test. Snapshots of the crack propagation for different values of the X^2 -displacement of Point A. The snapshots correspond to computations performed with the Saint-Venant Kirchhoff constitutive model.

in the X^2 -direction, which agrees well with the ones reported in [25]. In Fig. 8 we compare the propagation length predicted by Saint-Venant Kirchhoff and Neo-Hookean constitutive models, in which both models deliver similar propagation curves.

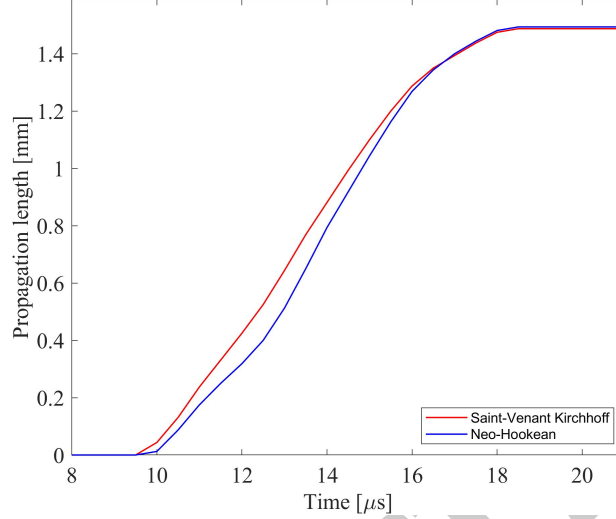


Figure 8: Symmetric three point bending test. Evolution of the propagation length of the crack for the Saint-Venant Kirchhoff and Neo-Hookean constitutive models.

5.2. Asymmetric three point bending test

Here, we model the asymmetric three point bending test [25, 27, 62]. The boundary conditions are similar to the previous case and are given in Fig. 9. The geometric properties and material parameters are adopted as $L_x = 20$ mm, $L_y = 8$ mm, $L_z = \Delta x$, $\lambda = 12$ GPa, $\mu = 8$ GPa, $\rho_0 = 1190$ kg/m³, and $G_c = 1$ kJ/m². We model the preexisting crack by restricting the neighbour search of the particles around the discontinuity region. The contact force is applied in the X^2 -direction with contact parameters of $K_p = 12 \times 10^{12}$ and $r_0 = 2.5\Delta x$. Other simulation parameters are set to $\epsilon_0 = \Delta x$, $\Delta t = 0.1$ ns, $\beta_1 = 0.2$, $\beta_2 = 0$, and $s_l = 0.1$. The Saint-Venant Kirchhoff constitutive model is employed. Fig. 10 shows the snapshots of the phase field for the deformed plate at different stages of the propagation. As can be seen, the crack initiation occurs when point A has displaced by approximately 0.17 mm in the X^2 -direction. Then, the crack joins the middle hole after a displacement of approximately 0.21 mm, and the complete rupture is recorded at a displacement of around 0.325 mm. The crack first propagates on a somewhat curved path from the preexisting crack tip to the middle hole, and then on an almost linear path until the full rupture. Fig. 11 compares the experimentally [62] and numerically [25, 27] obtained crack paths with the one predicted by the present TLSPH-phase field approach. As can be seen, the predicted crack path agrees very well with both the experimental and numerical studies found in the literature. There is

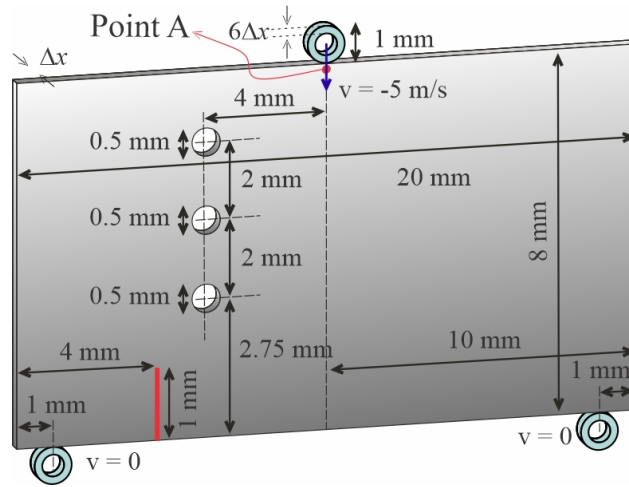


Figure 9: Asymmetric three point bending test. Geometry and loading conditions.

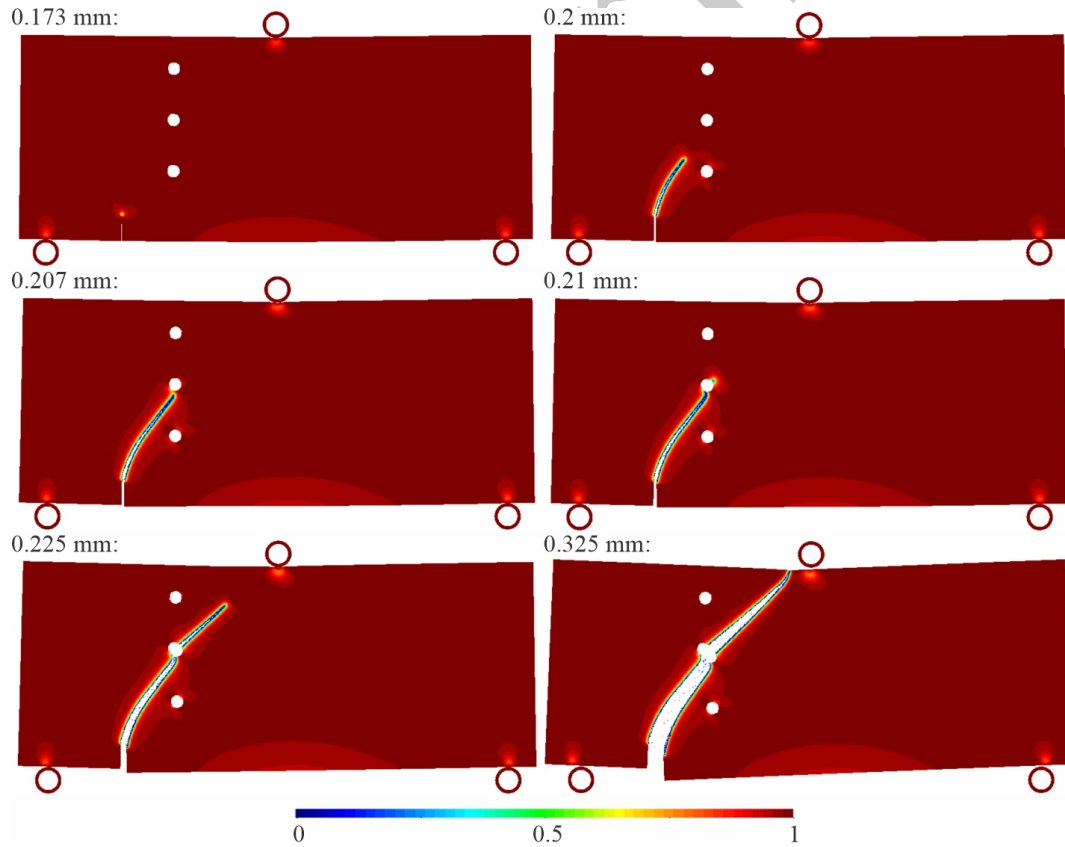


Figure 10: Asymmetric three point bending test. Snapshots of the crack propagation for different values of the X^2 -displacement of Point A.

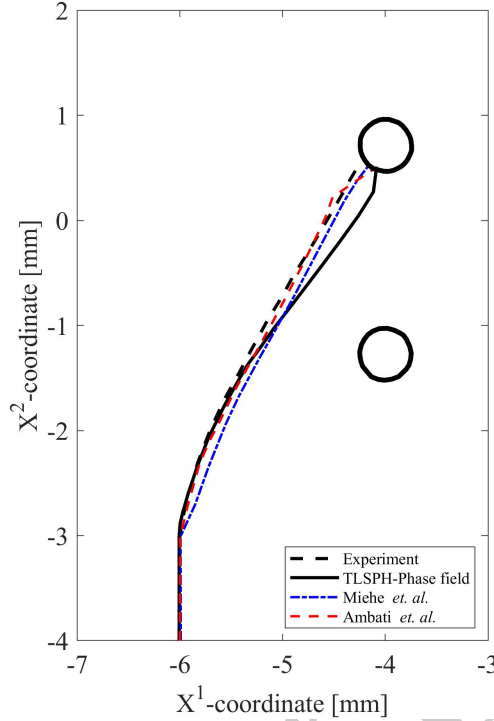


Figure 11: Asymmetric three point bending test. Crack path compared with experimental [62] and numerical [25, 27] studies.

a small deviation observed within a small region near the middle hole. One potential reason for this could be the imperfect representation of the circular holes in the discretized particle domain, which can alter the local strain energy concentrations. Nevertheless, the recorded deviation is negligible and does not change the overall physical behavior of the crack.

5.3. Dynamic crack branching

The dynamic crack branching problem has been widely investigated for different boundary conditions and loading setups [26, 42, 57, 63, 64]. In the present effort we focus on the setup used in [26, 42, 57], where a plate with a notch is subjected to a tensile surface loading. We set the material properties of the plate to $E = 32$ GPa, $\rho = 2450$ kg/m³, $\nu = 0.2$, and $G_c = 3$ J/m², whereas the Saint-Venant Kirchhoff constitutive model is employed. The length, width, and thickness of the plate are taken as $L_x = 100$ mm, $L_y = 40$ mm, and $L_z = \Delta x$, respectively. The preexisting notch is introduced as a geometrical discontinuity with a width of $4\Delta x$ and length of 50 mm located at the center. The plate is assumed to be under a tensile load of 1 MPa applied to its upper and lower surfaces, as depicted in Fig. 12. The length scale and time step values are set to $\epsilon_0 = 0.09375$ mm and $\Delta t = 2.5$ ns, respectively. We set the artificial viscosity parameters (see Section 2.3) to $\beta_1 = 0.04$ and $\beta_2 = 0$, and a phase field limit of $s_l = 0.1$ is chosen for soft particles.

To demonstrate the resolution independence of the crack pattern in the phase field method, we

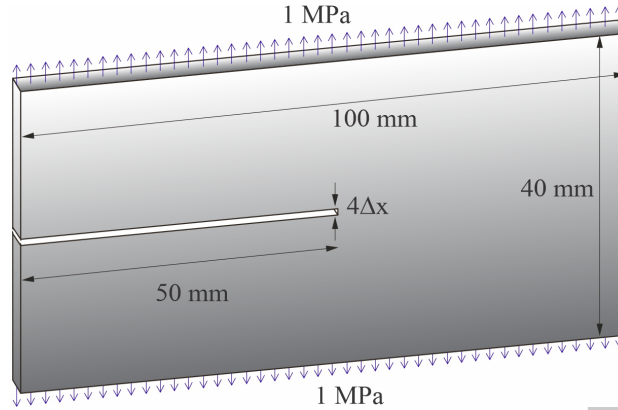


Figure 12: Dynamic crack branching. Geometry and loading conditions.

consider four different particle resolutions¹, R1-R4, with initial particle spacing of $\Delta x = 0.1$ mm, $\Delta x = 0.08$ mm, $\Delta x = 0.0625$ mm, and $\Delta x = 0.05$ mm, leading to a discretization of the domain into 398,000, 622,500, 1,020,800, and 1,596,000 particles, respectively.

Fig. 13 presents several snapshots of the phase field contours for R1-R4 resolutions at different stages of the crack propagation for the right half of the plate (the left half stays intact and we therefore omit that region). The crack propagation starts from the tip of the notch at approximately $t = 10 \mu s$ and continues in a horizontal manner. At approximately $t = 50 \mu s$, branching occurs, and the fracture propagates at an angle of $\approx 37^\circ$. At later stages, the propagation angles of the two branches tend to change back to horizontal. As expected, an identical crack pattern is predicted for all different resolutions, highlighting phase field's feature of mesh independence, which is hard to achieve when local damage models are employed. At the same time, the predicted crack patterns are in excellent agreement with the ones reported in [26, 42, 57]. However, the crack in resolutions R1 and R2 fails to reach the end of the plate in the given time. This is a common behavior seen for low discretization resolutions and it is attributed to the fact that for lower resolutions the fracture zone is slightly wider and hence there is more fracture energy per unit length. Similar behavior was also reported in [26, 42, 57]. Fig. 14 compares the propagation speed of the crack predicted by the current TLSPH-Phase field model with the ones of [26, 57]. A close agreement is observed between the results predicted by TLSPH-Phase field and the ones of [57]. In [26], however, a

¹Care should be taken when choosing the minimal resolution and time step. Although the crack path in phase field is independent of the resolution, extremely low particle resolutions may alter the path of the crack because the fracture energy is regularized over a larger length scale (cracks are wider), which can in turn affect the physics of the problem. Additionally, in TLSPH, for lower resolutions and large time step values, higher amount of artificial viscosity is needed to overcome the zero-energy mode discrepancy [56], thus, leading to a higher amount of nonphysical forces in the domain. This can then alter the original speed of the propagation, and in some cases even the path.

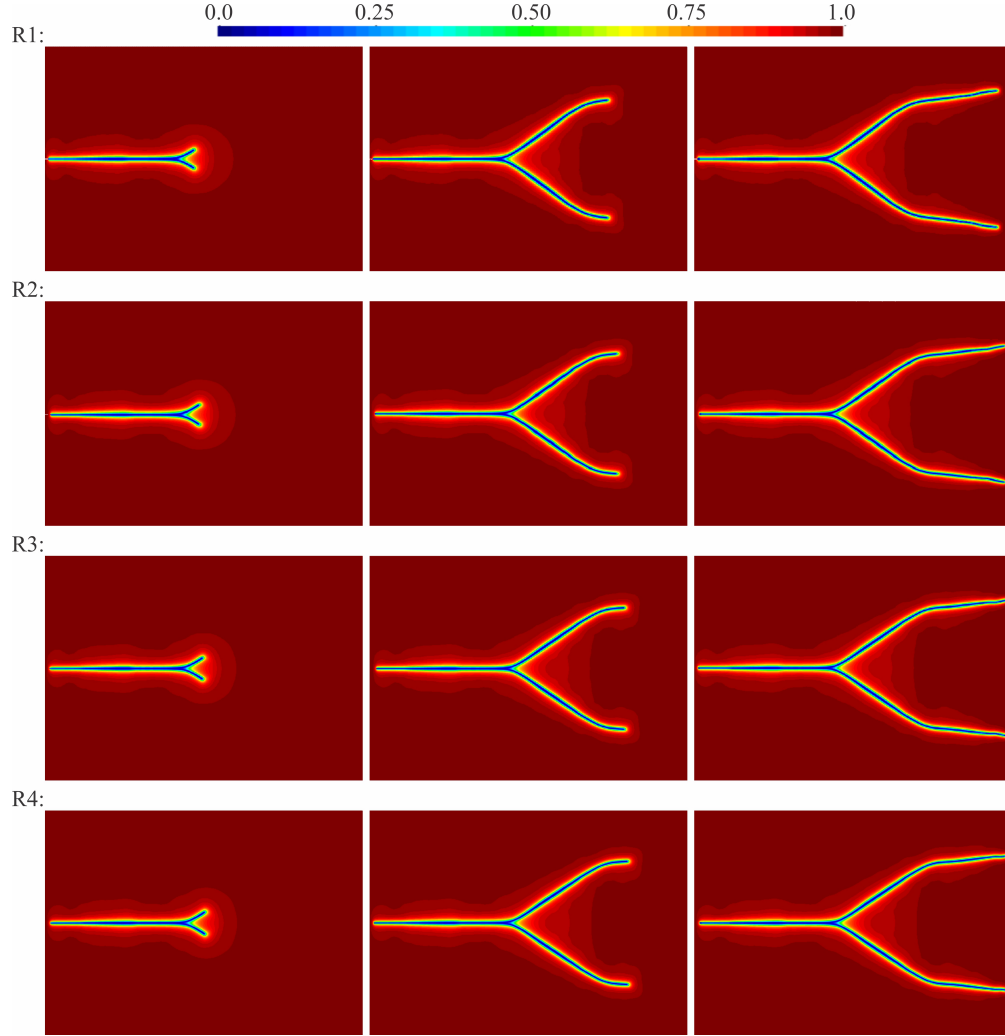


Figure 13: Dynamic crack branching. Contours of the phase field parameter at 55 μ s (left), 80 μ s (middle), and 105 μ s (right), for R1-R4 resolutions. The snapshots are presented for the right half of the plate.

slightly higher propagation speed is reported. This difference is attributed to the absence of the inertia term (\ddot{s}) in the phase-field PDE utilized in [26] (see Section 3). Obviously, the inclusion of the inertia term in the current effort (i.e. the use of a hyperbolic phase field PDE instead of an elliptic one, as described in Section 3) introduces an extra amount of work to be carried out in order for the phase field to propagate, thereby causing a decrease in the propagation speed. It is

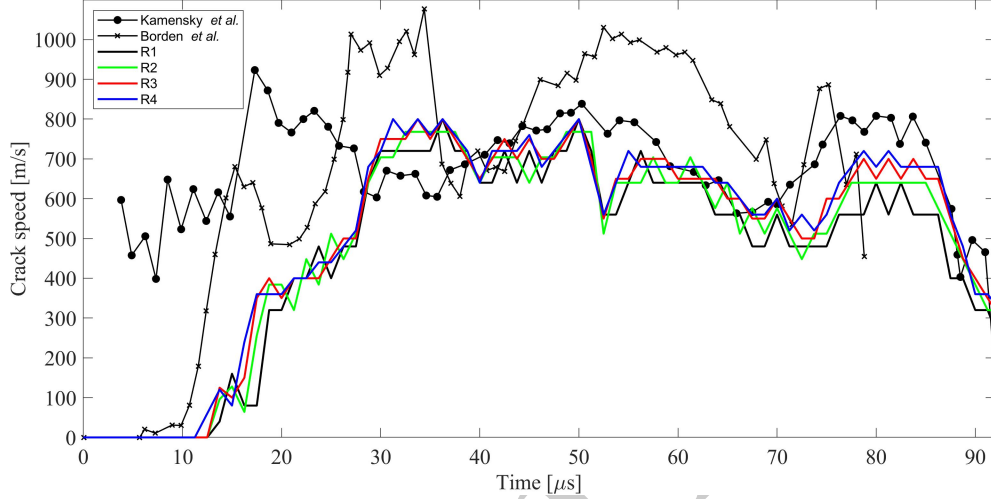


Figure 14: Dynamic crack branching. X^1 - component of crack velocity for resolutions R1-R4 compared with Kamensky *et al.* [57] and Borden *et al.* [26].

also worth mentioning that the strategy employed to track the crack tip, and hence the propagation speed, highly affects the recorded crack initiation time. Here, we consider the furthest particle in the $+X^1$ -direction with a phase field value of $s < 0.7$ to be the tip of the crack. Therefore, as soon as the phase field value decreases to 0.7, the propagation is assumed to initiate. However, the choice of this value does not affect the computed propagation speed since the speed is computed between the two iso-curves of the same value.

In Fig. 15 the post-processed final results of the phase field and the crack opening are given for resolution R4, where the particles with $s < s_l = 0.1$ are not shown, and the deformation is scaled by a factor of 50. As can be seen, after the complete failure, the domain separates into three regions, marking the end of the propagation.

5.4. Kalthoff–Winkler experiment

Here we revisit the well-known Kalthoff-Winkler experiment where a plate is subjected to an impact shear loading [65]. The length, width, and thickness of the plate, are adopted from [26, 42, 57] as $L_x = 100$ mm, $L_y = 100$ mm, and $L_z = \Delta x$, respectively. The material properties are set to $E = 190$ GPa, $\rho = 8000$ kg/m³, $\nu = 0.3$, $G_c = 22.13$ kJ/m², and the Saint-Venant Kirchhoff constitutive model is employed. The domain is discretized into 638,400 particles with an initial

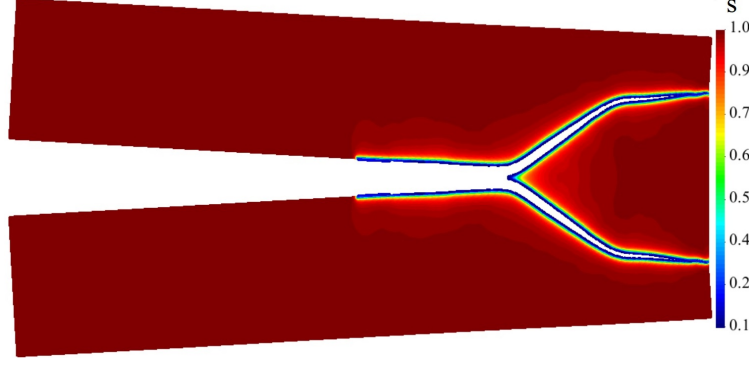


Figure 15: Dynamic crack branching. Opening of the crack and phase field distribution at the failure moment ($\approx 105 \mu s$) for resolution R4. Particles with $s < s_l = 0.1$ are not shown. The deformation is magnified by a factor of 50.

particle spacing of $\Delta x = 0.125$ mm. The length scale, time step, artificial viscosity parameters, and phase field limit for the soft particles, are chosen as $\epsilon_0 = 0.125$ mm, $\Delta t = 1.0$ ns, $\beta_1 = 0.04$ and $\beta_2 = 0$, and $s_l = 0.1$, respectively. A geometrical discontinuity with a width of $4\Delta x$ and length of 50 mm is introduced in the left side of the plate to model the preexisting notch, as shown in Fig. 16. The plate is subject to an impact loading in the horizontal direction, applied to the

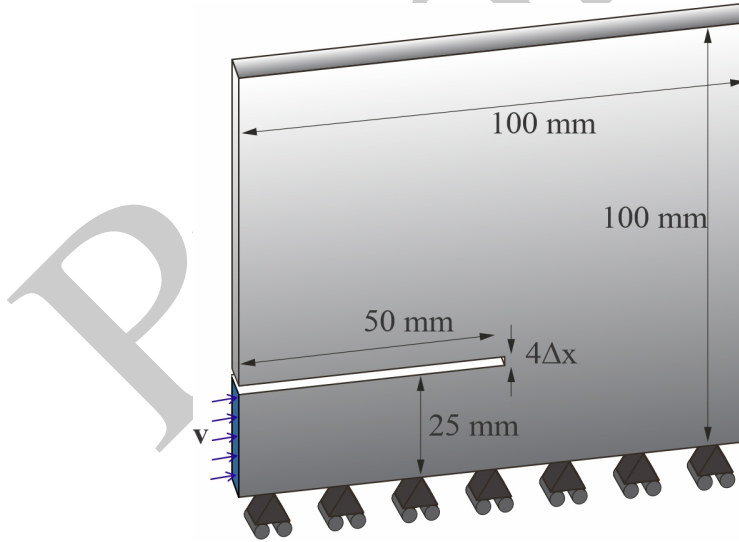


Figure 16: Kalthoff-Winkler experiment. Geometry and loading conditions.

particles located at the lower portion of the left surface. The loading condition is applied as a time-dependent ramp-up velocity of

$$v = \begin{cases} \frac{t}{t_0} 16.5 \text{ m/s} & t \leq t_0 \\ 16.5 \text{ m/s} & \text{otherwise} \end{cases}, \quad (77)$$

in the X^1 -direction, where $t_0 = 1 \mu\text{s}$ is the ramp-up time. Upon impact ($t = 0$), the displacement field starts propagating towards the right, eventually causing stress and strain energy concentrations at the notch tip, which are then dissipated by the propagating crack (or phase field). Fig. 17 shows the snapshots of the TLSPH-Phase field results for different stages of the propagation. The crack propagation starts at approximately $25 \mu\text{s}$ and continues diagonally until the full rapture at approximately $100 \mu\text{s}$. A local disturbance in the diagonal path of the crack is recorded between $t \approx 63 \mu\text{s}$ and $t \approx 75 \mu\text{s}$ (marked in Circle A in Fig. 17) which implies a mixed mode I-II fracture (also reported in [26, 42, 57]). Fig. 18 compares the propagation speed and crack orientation

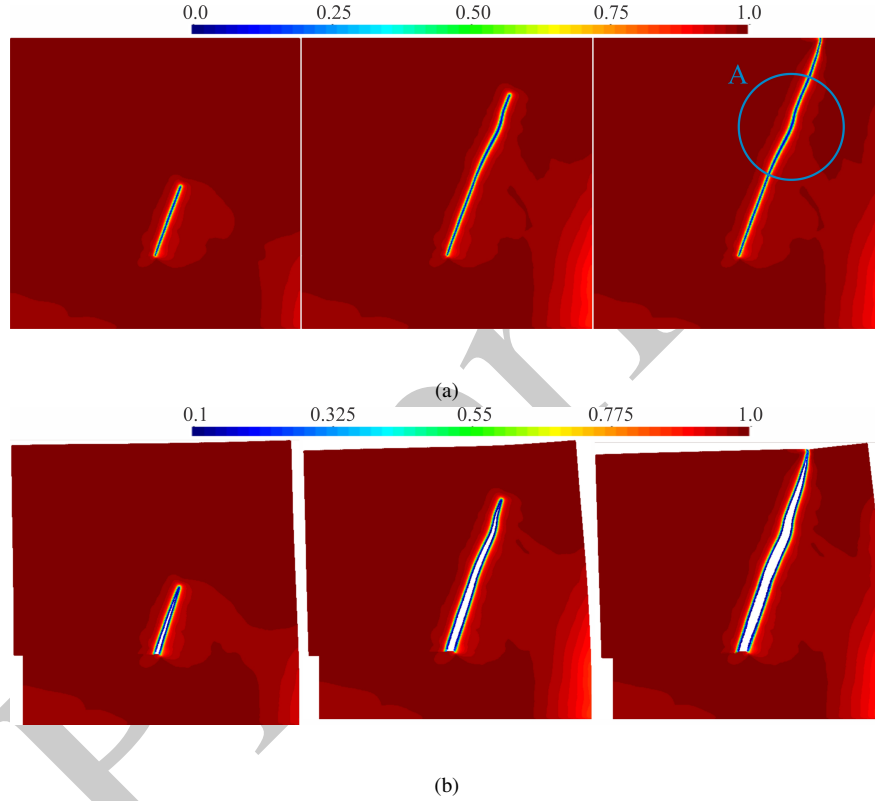


Figure 17: Kalthoff-Winkler experiment. a) The phase field and b) opening of the crack at $50 \mu\text{s}$ (left), $80 \mu\text{s}$ (middle), and $101 \mu\text{s}$ (right). In b), particles with $s < s_l = 0.1$ are not shown and the deformation is magnified by a factor of 5.

predicted by the current TLSPH-Phase field approach with the ones of the elliptic phase field [26] and peridynamic [66] models. Due to the explicit nature of the present computations, the graph is smoothed. The portion belonging to the disturbance region (Circle A) is marked with gray color. The predicted results of crack propagation and orientation, as well as the elastodynamic behavior of the plate, are in good agreement with different numerical models and the corresponding experimental work. The TLSPH-Phase field model is able to precisely capture all the complex qualitative and quantitative characteristics of the crack at different stages.

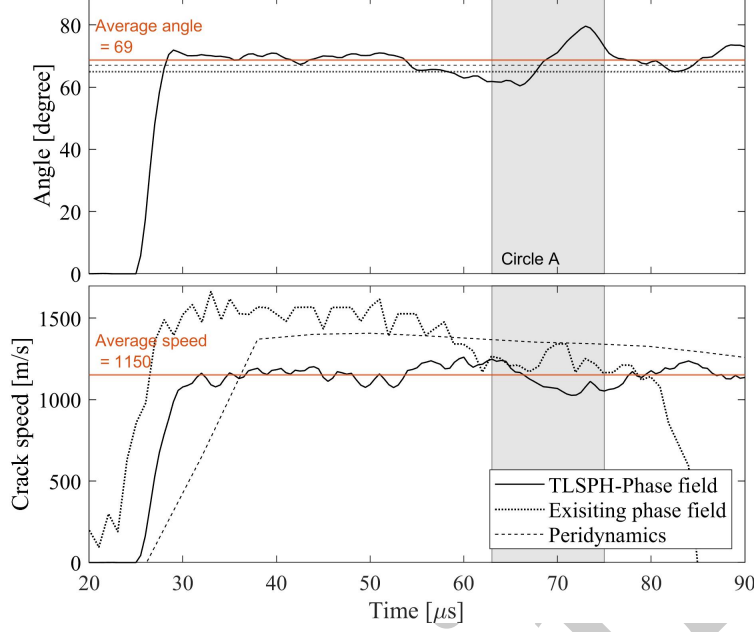


Figure 18: Kalthoff-Winkler experiment. TLSPH-Phase field results of the propagation speed and orientation of crack compared to existing phase field [26] and peridynamic [66] models.

5.5. Notched plate with hole

In this example, we simulate the interaction of cracks with other structural defects in a porous plate with an eccentric hole. The geometry of the plate is provided in Fig. 19, where the thickness is Δx . The material properties are set to $\lambda = 1.94$ GPa, $\mu = 2.45$ GPa, $\rho = 2000$ kg/m³, $G_c = 2.28$ kJ/m², and the Saint-Venant Kirchhoff constitutive model is employed. The domain is discretized into 732,852 particles with an initial particle spacing of $\Delta x = 0.1$ mm. The length scale, time step, artificial viscosity parameters, and phase field limit for the soft particles, are chosen as $\epsilon_0 = 0.1$ mm, $\Delta t = 4.0$ ns, $\beta_1 = 0.04$ and $\beta_2 = 0$, and $s_l = 0.1$, respectively. The original experiment [27] was performed in a displacement-control manner, where a prescribed displacement rate of 0.1 mm/min was applied. The corresponding simulations [27, 29, 67] were carried out under static displacement loading condition. For both the experiment and the simulations, the prescribed displacement was applied to the upper hole (colored in blue in Fig. 19) of the plate, while the lower hole (colored in red in Fig. 19) was fixed in the horizontal and vertical directions. Here, due to the explicit nature of the SPH method, we conduct dynamic simulations, with three different cases of prescribed velocity in the vertical direction; $v = 0.5$ m/s, 0.2 m/s, 0.1 m/s, applied on two layers of particles around the upper hole, whereas the two layers of particles around the lower hole are fixed in the X^1 - and X^2 -directions. A preexisting crack with a length of 10 mm is located in the left-central portion of the plate, as shown in Fig. 19, and is modeled by restricting the neighbour search of the particles around the discontinuity region, as suggested in Section 4.3

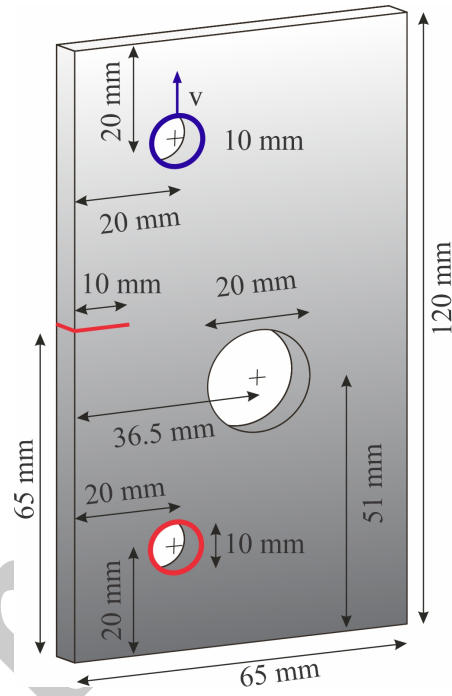


Figure 19: Notched plate with hole. Geometry and loading conditions. The particles around the lower hole (colored in red) are fixed in the X^1 - and X^2 -directions, and the prescribed velocity condition is applied to the particles around the upper hole (colored in blue) in the X^2 -direction. The preexisting crack with a length of 10 mm can be seen in red 65 mm from the bottom edge of the specimen.

and Fig. 4d.

The crack initiation is observed after the upper hole has displaced by approximately 0.3 mm in the X^2 -direction for all three cases of the prescribed velocity. The presence of the eccentric hole forms a weak-zone in the vicinity of the crack tip which generates the so-called accelerating effect on the propagating crack [63, 68]. As a result, the crack path is directed towards the hole, and eventually joins the hole after a displacement of approximately 0.4 mm. Upon joining the hole the crack dissipates its energy, leading to a significant delay in propagation, caused by the arresting effect of the hole. At a displacement of approximately 1.4 mm, a new crack initiates from the right side of the hole and causes a fast and complete rupture. The complex physics in terms of the accelerating and arresting effects of the hole on the crack are well-captured by the present TLSPH-Phase field approach. Identical accelerating and arresting effects were reported in [63, 68] using peridynamics. Fig. 20 depicts the snapshots of the final crack pattern under different prescribed velocity loading conditions. As it is seen, the present approach is able to capture all

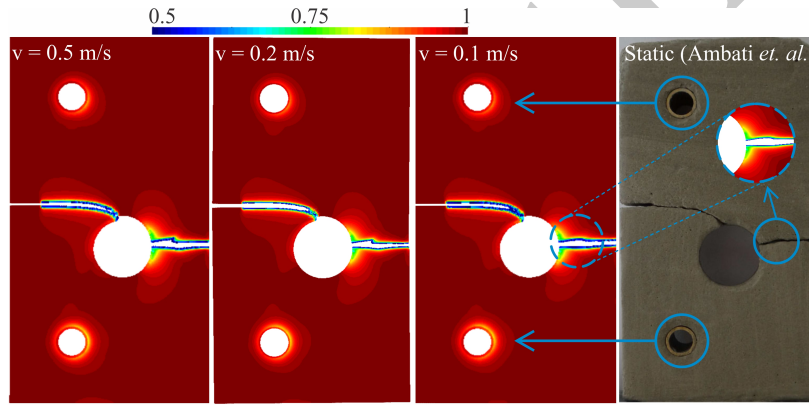


Figure 20: Notched plate with hole. Comparison of the final crack pattern versus the experimental results of Ambati *et al.* [27]. Particles with $s < 0.5$ are not shown.

the major qualitative features of fracture, such as the damaged region around the supports, as well as the tendency of the crack to branch in the vicinity of the eccentric hole (marked with circles in Fig. 20), which demonstrates a good agreement with the experimental results of [27]. A small deviation of the crack path in terms of small branching is observed for higher prescribed velocity values. This is in agreement with the reported effects of the dynamic loading on crack branching [69] and the experimental observations in [27]. Fig. 21 compares the phase field values for different loading conditions at various stages of the propagation. As can be seen, for lower values of the prescribed velocity, the branching effect close to the hole vanishes, which agrees well with the findings of [69]. Fig. 22 presents the smoothed graph of the reaction force (at the lower hole) versus maximum displacement (displacement of the upper hole) for $v = 0.1 \text{ m/s}$. We would like to point out that although this problem has been investigated by several researchers in the past

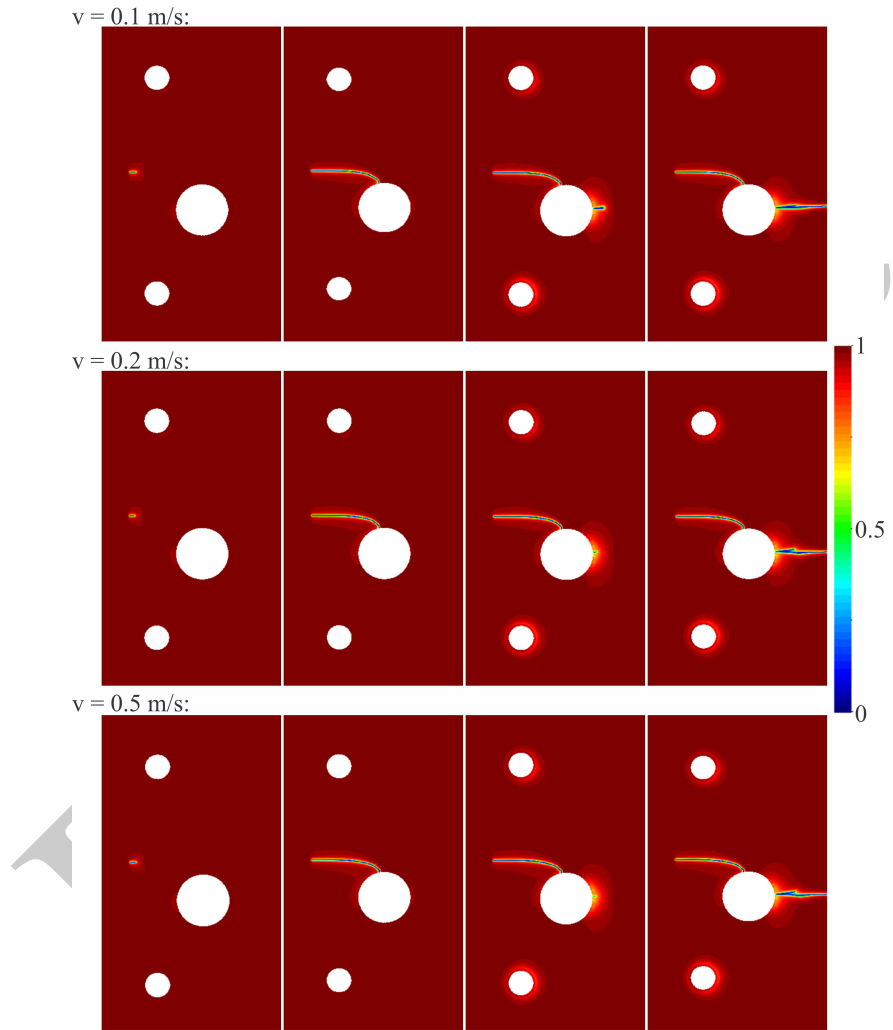


Figure 21: Notched plate with hole. Snapshots of the phase field under different velocity loading conditions for upper hole displacement values of 0.3 mm (first column), 0.42 mm (second column), 1.42 mm (third column), and 1.48 mm (fourth column).

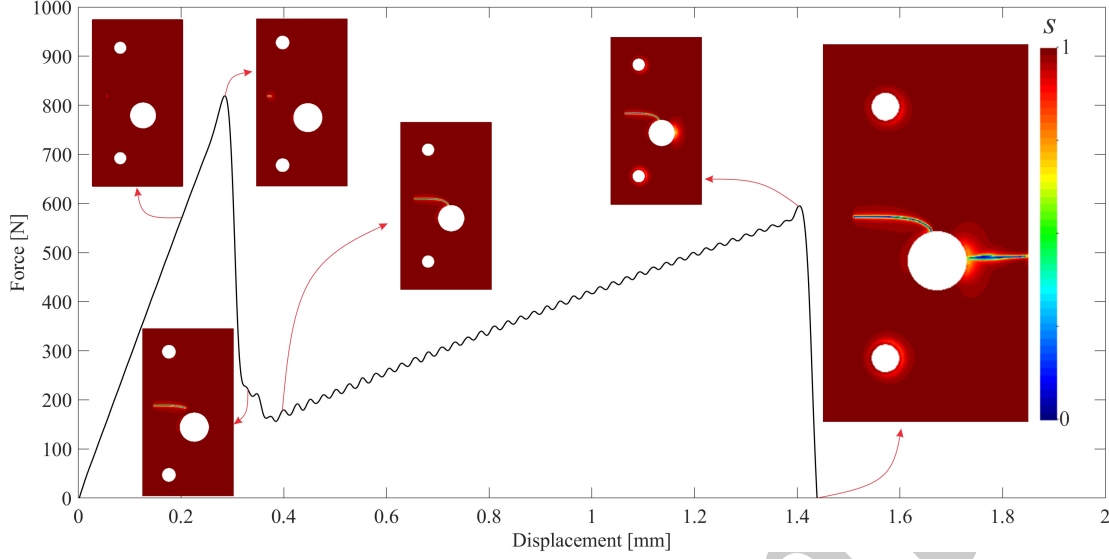


Figure 22: Notched plate with hole. Reaction force-displacement graph for $v = 0.1$ m/s. Snapshots of the crack at various stages are superimposed for a comparative view.

[27, 29, 67], the corresponding reaction force - displacement graphs are not in agreement among each other. Furthermore, all the previous works, in contrast to the present effort, solved the problem in a static manner. Hence, some discrepancies are expected in the reaction force - displacement curve. However, the qualitative features of the graph are captured well. Moreover, the time at which the first crack initiation occurs (sudden drop in the curve at approximately 0.3 mm) is in excellent agreement with the one reported in [29, 67]. Finally, it should be pointed out that the oscillations appearing from approximately 0.4 mm to 1.4 mm are attributed to the dynamic nature of the numerical simulation.

5.6. Impact of a spherical projectile on a notched circular plate

To further demonstrate the capabilities of our proposed framework we simulate the impact of a rigid spherical projectile on a notched circular plate. Fig. 23 illustrates the geometric properties of the domain in which the diameter and thickness of the plate are given as $37\Delta x$ and $5\Delta x$, respectively. A rigid spherical projectile with a diameter of $16\Delta x$ and a prescribed velocity of -10 m/s in the X^3 -direction impacts the plate at time $t = 0$. A through-the-thickness cross-shaped notch with side lengths of $18\Delta x$ is applied at the center of the plate and is modeled by restricting the neighbour search of the particles around the notch. We set the material and simulation parameters to $\lambda = 4.75$ GPa, $\mu = 0.9$ GPa, $\rho_0 = 1200$ kg/m³, $G_c = 703$ J/m², $\epsilon_0 = \Delta x$, $\Delta t = 2.5$ ns, $\beta_1 = 0.05$, $\beta_2 = 0$, $s_l = 0.1$, $r_0 = 2\Delta x$, and $K_p = 1.2 \times 10^{12}$. The domain is discretized into 800,774 particles with a particle spacing of $\Delta x = 0.165$ mm and the results are obtained using the Neo-Hookean constitutive model. Fig. 24 and Fig. 25 show the three- and two- dimensional

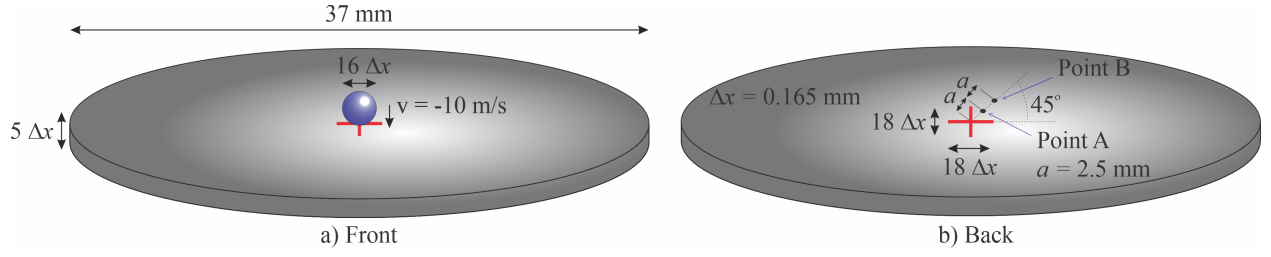


Figure 23: Impact of a spherical projectile on a notched circular plate. Geometry and loading conditions.

views of the phase field in the deformed plate, respectively. As can be seen, upon impact the

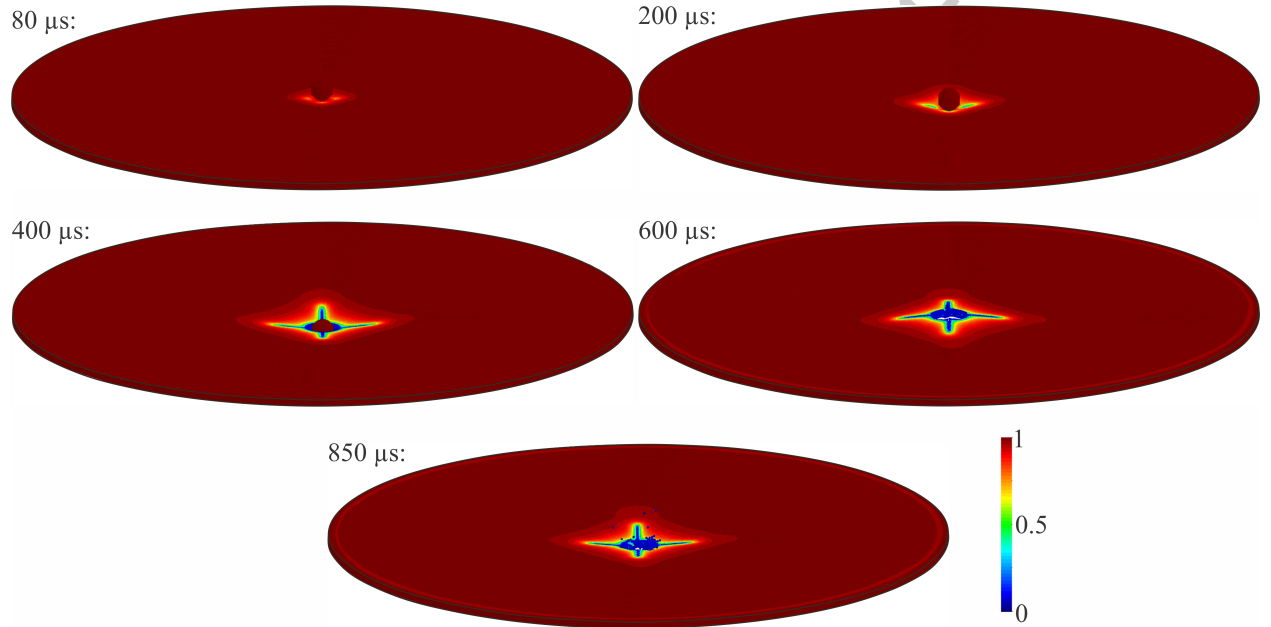


Figure 24: Impact of a spherical projectile on a notched circular plate. Three dimensional view of the phase field.

plate starts to deform, and after approximately $80 \mu s$ the propagation initiates from the back side of the preexisting notch tips. Since the back side of the plate undergoes higher tension than the front, the propagation at the back starts earlier. At later stages of the propagation, the plate is forced to break from the boundaries of the weak regions under high tension which correspond to the regions under the impact of the projectile, thus, leading to an ultimate penetration. After the penetration, the plate bounces back and dissipates its accumulated strain energy marking the end of crack propagation. Fig. 26 shows the displacements of Point A and Point B (see Fig. 23) in the X^3 -direction with respect to time. As can be seen, the proposed approach is able to efficiently capture the pre- and post-failure behaviors of the complex contact problem with complex fracture patterns. This problem is merely a demonstration of capabilities, and although neither experimental nor numerical results exist for comparison purposes, all the qualitative features that are expected from

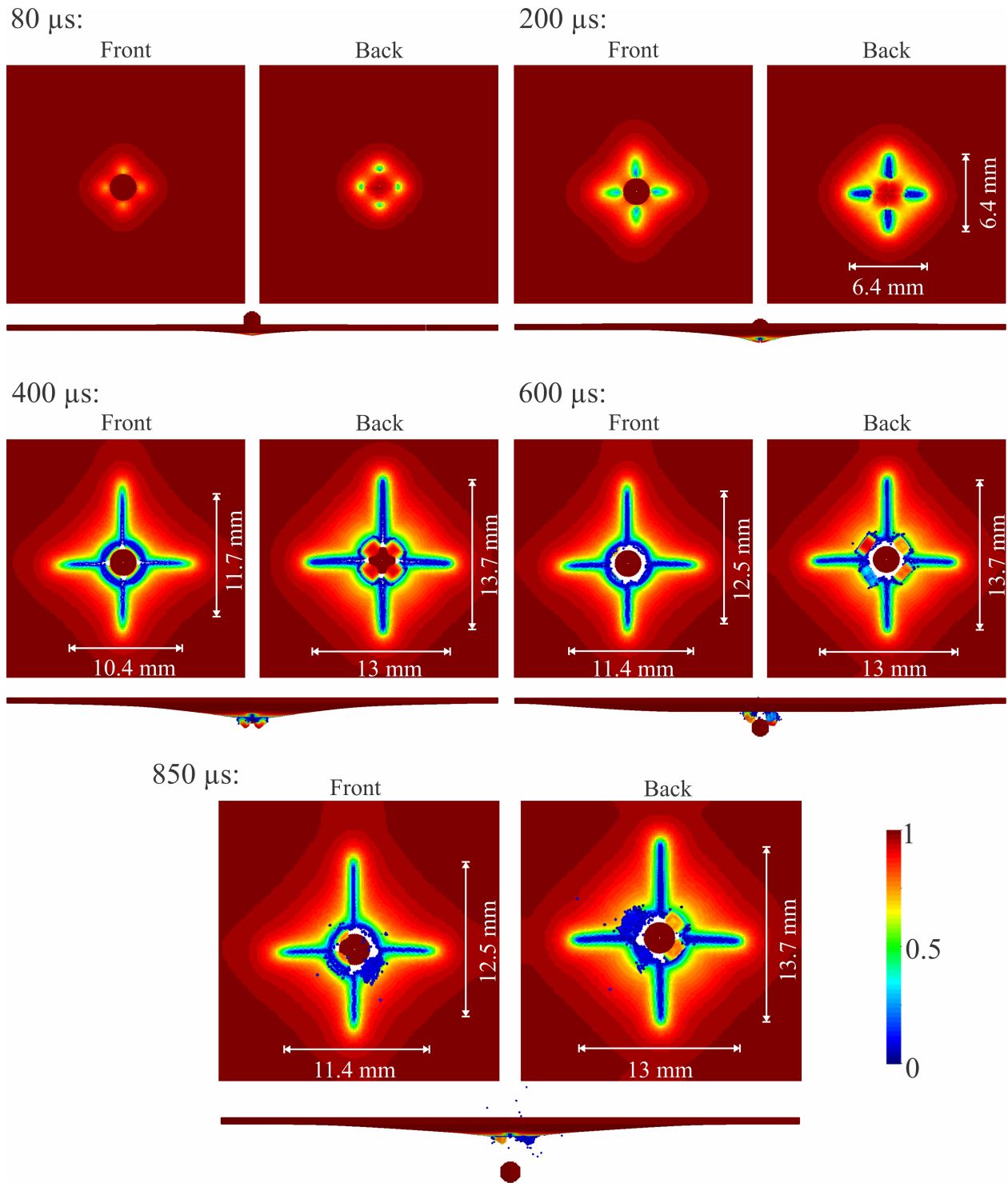


Figure 25: Impact of a spherical projectile on a notched circular plate. Two dimensional view of the phase field.

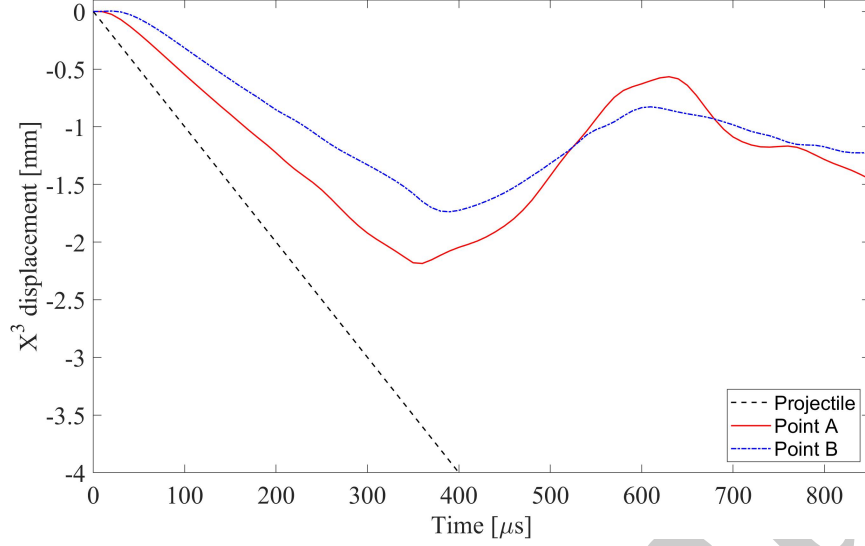


Figure 26: Impact of a spherical projectile on a notched circular plate. Displacements of Point A and Point B in the X^3 -direction.

the underlying physics are produced.

6. Conclusions

We presented a robust, accurate, and convergent computational framework for modeling dynamic brittle fracture within the SPH method. The proposed approach combines the well-known SPH numerical framework with a recently developed hyperbolic model for phase field of brittle fracture. The use of SPH allows for the simulation of large deformation problems that potentially involve multi-body interactions, whereas the use of a hyperbolic PDE for the phase field governing equation permits explicit integration in time, without having to solve expensive linear systems associated with elliptic models, or introduce severe time step restrictions associated with parabolic models.

The results of fracture analyses performed using the proposed formulation are in excellent agreement with solutions calculated using standard mesh-based numerical techniques, such as the finite element method and isogeometric analysis. At the same time, they are in very good agreement with results from experimental studies. The last numerical example, although it does not have any corresponding experimental or numerical results, is a demonstration-of-capabilities study, and produces all the qualitative features that are expected from the underlying physics.

This proof-of-concept work presents the core formulation of the coupled TLSPH-Phase field framework. Immediate future efforts will focus on large deformation fluid–structure interaction problems, functionally graded materials, as well as parallelization based on graphics processing units (GPU).

Acknowledgments

We wish to thank the Institute for Advanced Computational Science (IACS) at Stony Brook University for providing HPC resources that have contributed to the research results reported within this paper.

Appendix A. Interface force for contact problems in SPH

In a typical contact problem in SPH an additional term arising from the contact of two separate bodies is included in the governing equation. Thus, the resulting momentum equation (Eq.(17)) becomes

$$\frac{dv_i^k}{dt} = \sum_{j=1}^{N_i} m_{0j} \left(\frac{P_i^{ks}}{\rho_{0i}^2} + \frac{P_j^{ks}}{\rho_{0j}^2} + P_{vij}^{ks} \right) \frac{\partial W_{0ij}}{\partial X_j^s} + b_{0i}^k + \sum_{a=1}^{\hat{N}_i} f_{ai} r_{ai}^k. \quad (A.1)$$

In the newly included term, \hat{N}_i is the total number of particles located at a separate body within the contact distance of particle i , r_{ai}^k is the k component of the relative position vector $\mathbf{r}_{ai} = \mathbf{x}_a - \mathbf{x}_i$ between particles a and i calculated using the eulerian coordinates \mathbf{x} (see Fig. 5), and f_{ai} is a scalar multiplier. Borrowing mostly from [70] we calculate f_{ai} as

$$f_{ai} = \frac{m_{0a} K_p}{|\mathbf{r}_{ai}|^2} \begin{cases} B_{ai} R_{ai} & |\mathbf{r}_{ai}| \leq r_0 \\ 0 & \text{otherwise} \end{cases}, \quad (A.2)$$

where

$$B_{ai} = \frac{1 + \frac{|\mathbf{r}_{ai}|}{r_0}}{1 - e} \left(e^{1 + \frac{|\mathbf{r}_{ai}|}{r_0}} - 1 \right), \quad (A.3)$$

$$R_{ai} = \begin{cases} \frac{(1+1.5\tilde{q})(2-\tilde{q})^3}{8} & \frac{d(|\mathbf{r}_{ai}|)}{dt} \leq 0 \\ 0 & \text{otherwise} \end{cases}, \quad (A.4)$$

$$\tilde{q} = \frac{|\mathbf{r}_{ai}|}{1.33\Delta x}. \quad (A.5)$$

m_{0a} is the initial mass of particle a , r_0 is the contact distance, and K_p is a constant determining the potential of the contact.

Appendix B. Supplementary data

Supplementary material related to this article can be found online at [“DOI LINK FOR VIDEOS”](#).

References

- [1] Robert A Gingold and Joseph J Monaghan. Smoothed particle hydrodynamics: theory and application to non-spherical stars. *Monthly Notices of the Royal Astronomical Society*, 181(3):375–389, 1977.
- [2] L. B. Lucy. A numerical approach to the testing of the fission hypothesis. *The Astronomical Journal*, 82(12):1013–1024, 1977.
- [3] J.J. Monaghan. Simulating free surface flows with sph. *Journal of Computational Physics*, 110(2):399–406, 1994.
- [4] Larry Libersky and A. Petschek. *Smooth particle hydrodynamics with strength of materials*, in *Advances in the Free-Lagrange Method*, volume 395, pages 248–257. 01 2006.
- [5] J.W. Swelge, D.L. Hicks, and S.W. Attaway. SPH Stability Analysis. *Journal of Computational Physics*, 116:123–134, 1995.
- [6] C.T. Dyka and R.P. Ingel. An approach for tension instability in smoothed particle hydrodynamics (sph). *Computers & Structures*, 57(4):573–580, 1995.
- [7] J. Bonet and T. S.L. Lok. Variational and momentum preservation aspects of Smooth Particle Hydrodynamic formulations. *Computer Methods in Applied Mechanics and Engineering*, 180(1-2):97–115, 1999.
- [8] J. J. Monaghan. Smoothed particle hydrodynamics. *Reports on Progress in Physics*, 68(8):1703–1759, 2005.
- [9] Juan R. Reveles. *Development of a total Lagrangian SPH code for the simulation of solids under dynamic loading*. PhD thesis, Cranfield University, 2007.
- [10] MB Liu and GR2593940 Liu. Smoothed particle hydrodynamics (sph): an overview and recent developments. *Archives of Computational Methods in Engineering*, 17(1):25–76, 2010.
- [11] Leonardo Di G. Sigalotti, Jaime Klapp, Otto Rendón, Carlos A. Vargas, and Franklin Peña-Polo. On the kernel and particle consistency in smoothed particle hydrodynamics. *Applied Numerical Mathematics*, 108:242–255, 2016.
- [12] Shan Qun Chen, Bin Liao, and Tao Huang. Corrected SPH methods for solving shallow-water equations. *Journal of Hydrodynamics*, 28(3):389–399, 2016.

- [13] M. Naqib Rahimi, Deniz Can Kolukisa, Mehmet Yildiz, Murat Ozbulut, and Adnan Kefal. A generalized hybrid smoothed particle hydrodynamics–peridynamics algorithm with a novel lagrangian mapping for solution and failure analysis of fluid–structure interaction problems. *Computer Methods in Applied Mechanics and Engineering*, 389:114370, 2022.
- [14] Timon Rabczuk and J Eibl. Simulation of high velocity concrete fragmentation using sph/mlsph. *International Journal for Numerical Methods in Engineering*, 56(10):1421–1444, 2003.
- [15] Sukanta Chakraborty and Amit Shaw. A pseudo-spring based fracture model for sph simulation of impact dynamics. *International Journal of Impact Engineering*, 58:84–95, 2013.
- [16] Md Rushdie Ibne Islam and Chong Peng. A total lagrangian sph method for modelling damage and failure in solids. *International Journal of Mechanical Sciences*, 157:498–511, 2019.
- [17] Md Rushdie Ibne Islam and Amit Shaw. Pseudo-spring sph simulations on the perforation of metal targets with different damage models. *Engineering Analysis with Boundary Elements*, 111:55–77, 2020.
- [18] Yingnan Wang, Ha H Bui, Giang D Nguyen, and PG Ranjith. A new sph-based continuum framework with an embedded fracture process zone for modelling rock fracture. *International Journal of Solids and Structures*, 159:40–57, 2019.
- [19] Yingnan Wang, Hieu T Tran, Giang D Nguyen, Pathegama G Ranjith, and Ha H Bui. Simulation of mixed-mode fracture using sph particles with an embedded fracture process zone. *International Journal for Numerical and Analytical Methods in Geomechanics*, 44(10):1417–1445, 2020.
- [20] Ha H Bui and Giang D Nguyen. Smoothed particle hydrodynamics (sph) and its applications in geomechanics: From solid fracture to granular behaviour and multiphase flows in porous media. *Computers and Geotechnics*, 138:104315, 2021.
- [21] T. Rabczuk and T. Belytschko. Cracking particles: a simplified meshfree method for arbitrary evolving cracks. *International Journal for Numerical Methods in Engineering*, 61(13):2316–2343, 2004.
- [22] Nicolas Moës, John Dolbow, and Ted Belytschko. A finite element method for crack growth without remeshing. *International Journal for Numerical Methods in Engineering*, 46(1):131–150, 1999.

- [23] Nicolas Moës and Ted Belytschko. Extended finite element method for cohesive crack growth. *Engineering Fracture Mechanics*, 69(7):813–833, 2002.
- [24] C Kuhn and R Müller. A phase field model for fracture. In *PAMM: Proceedings in Applied Mathematics and Mechanics*, volume 8, pages 10223–10224. Wiley Online Library, 2008.
- [25] Christian Miehe, Martina Hofacker, and Fabian Welschinger. A phase field model for rate-independent crack propagation: Robust algorithmic implementation based on operator splits. *Computer Methods in Applied Mechanics and Engineering*, 199(45-48):2765–2778, 2010.
- [26] Michael J. Borden, Clemens V. Verhoosel, Michael A. Scott, Thomas J.R. Hughes, and Chad M. Landis. A phase-field description of dynamic brittle fracture. *Computer Methods in Applied Mechanics and Engineering*, 217-220:77–95, 2012.
- [27] Marreddy Ambati, Tymofiy Gerasimov, and Laura De Lorenzis. A review on phase-field models of brittle fracture and a new fast hybrid formulation. *Computational Mechanics*, 55(2):383–405, 2015.
- [28] Jian-Ying Wu and Vinh Phu Nguyen. A length scale insensitive phase-field damage model for brittle fracture. *Journal of the Mechanics and Physics of Solids*, 119:20–42, 2018.
- [29] Adrian Egger, Udit Pillai, Konstantinos Agathos, Emmanouil Kakouris, Eleni Chatzi, Ian A. Aschroft, and Savvas P. Triantafyllou. Discrete and phase field methods for linear elastic fracture mechanics: A comparative study and state-of-the-art review. *Applied Sciences*, 9(12), 2019.
- [30] Jian-Ying Wu, Vinh Phu Nguyen, Chi Thanh Nguyen, Danas Sutula, Sina Sinaie, and Stéphane PA Bordas. Phase-field modeling of fracture. In *Advances in Applied Mechanics*, volume 53, pages 1–183. Elsevier, 2020.
- [31] Lampros Svolos, Curt A Bronkhorst, and Haim Waisman. Thermal-conductivity degradation across cracks in coupled thermo-mechanical systems modeled by the phase-field fracture method. *Journal of the Mechanics and Physics of Solids*, 137:103861, 2020.
- [32] Tushar Kanti Mandal, Vinh Phu Nguyen, Jian-Ying Wu, Chi Nguyen-Thanh, and Alban de Vaucorbeil. Fracture of thermo-elastic solids: Phase-field modeling and new results with an efficient monolithic solver. *Computer Methods in Applied Mechanics and Engineering*, 376:113648, 2021.
- [33] Lampros Svolos, Hashem M Mourad, Curt A Bronkhorst, and Haim Waisman. Anisotropic thermal-conductivity degradation in the phase-field method accounting for crack directionality. *Engineering Fracture Mechanics*, 245:107554, 2021.

- [34] Gilles A Francfort and J-J Marigo. Revisiting brittle fracture as an energy minimization problem. *Journal of the Mechanics and Physics of Solids*, 46(8):1319–1342, 1998.
- [35] Blaise Bourdin, Gilles A Francfort, and Jean-Jacques Marigo. Numerical experiments in revisited brittle fracture. *Journal of the Mechanics and Physics of Solids*, 48(4):797–826, 2000.
- [36] Alan Arnold Griffith. Vi. the phenomena of rupture and flow in solids. *Philosophical transactions of the royal society of London. Series A, containing papers of a mathematical or physical character*, 221(582-593):163–198, 1921.
- [37] Michael J Borden, Thomas JR Hughes, Chad M Landis, and Clemens V Verhoosel. A higher-order phase-field model for brittle fracture: Formulation and analysis within the isogeometric analysis framework. *Computer Methods in Applied Mechanics and Engineering*, 273:100–118, 2014.
- [38] Lin Chen, Bin Li, and René de Borst. Adaptive isogeometric analysis for phase-field modeling of anisotropic brittle fracture. *International Journal for Numerical Methods in Engineering*, 121(20):4630–4648, 2020.
- [39] Khuong D Nguyen, Cuong-Le Thanh, H Nguyen-Xuan, and Magd Abdel-Wahab. A hybrid phase-field isogeometric analysis to crack propagation in porous functionally graded structures. *Engineering with Computers*, pages 1–21, 2021.
- [40] Fatemeh Amiri, Daniel Millán, Marino Arroyo, Mohammad Silani, and Timon Rabczuk. Fourth order phase-field model for local max-ent approximants applied to crack propagation. *Computer Methods in Applied Mechanics and Engineering*, 312:254–275, 2016.
- [41] EG Kakouris and Savvas P Triantafyllou. Phase-field material point method for brittle fracture. *International Journal for Numerical Methods in Engineering*, 112(12):1750–1776, 2017.
- [42] Georgios Moutsanidis, David Kamensky, JS Chen, and Yuri Bazilevs. Hyperbolic phase field modeling of brittle fracture: Part II—immersed IGA–RKPM coupling for air-blast–structure interaction. *Journal of the Mechanics and Physics of Solids*, 121:114–132, 2018.
- [43] Emmanouil G Kakouris and Savvas P Triantafyllou. Phase-field material point method for dynamic brittle fracture with isotropic and anisotropic surface energy. *Computer Methods in Applied Mechanics and Engineering*, 357:112503, 2019.

- [44] Ngoc-Hien Nguyen, Vinh Phu Nguyen, Jian-Ying Wu, Thi-Hong-Hieu Le, Yan Ding, et al. Mesh-based and meshfree reduced order phase-field models for brittle fracture: One dimensional problems. *Materials*, 12(11):1858, 2019.
- [45] Yulong Shao, Qinglin Duan, and Shasha Qiu. Adaptive consistent element-free galerkin method for phase-field model of brittle fracture. *Computational Mechanics*, 64(3):741–767, 2019.
- [46] Weidong Li, Nhon Nguyen-Thanh, and Kun Zhou. Phase-field modeling of brittle fracture in a 3d polycrystalline material via an adaptive isogeometric-meshfree approach. *International Journal for Numerical Methods in Engineering*, 121(22):5042–5065, 2020.
- [47] Junchao Wu, Dongdong Wang, Zeng Lin, and Dongliang Qi. An efficient gradient smoothing meshfree formulation for the fourth-order phase field modeling of brittle fracture. *Computational Particle Mechanics*, 7(2):193–207, 2020.
- [48] Yulong Shao, Qinglin Duan, and Shasha Qiu. Adaptive analysis for phase-field model of brittle fracture of functionally graded materials. *Engineering Fracture Mechanics*, 251:107783, 2021.
- [49] Y. Krongauz and T. Belytschko. Consistent pseudo-derivatives in meshless methods. *Computer Methods in Applied Mechanics and Engineering*, 146(3-4):371–386, 1997.
- [50] J. P. Vila. On particle weighted methods and smooth particle hydrodynamics. *Mathematical Models and Methods in Applied Sciences*, 9(2):161–209, 1999.
- [51] Ted Belytschko, Yong Guo, Wing Kam Liu, and Shao Ping Xiao. A unified stability analysis of meshless particle methods. *International Journal for Numerical Methods in Engineering*, 48(9):1359–1400, 2000.
- [52] J.P. Morris. An overview of the method of smoothed particle hydrodynamics. ., 1995.
- [53] T. Rabczuk, T. Belytschko, and S. P. Xiao. Stable particle methods based on Lagrangian kernels. *Computer Methods in Applied Mechanics and Engineering*, 193(12-14):1035–1063, 2004.
- [54] Jun Lin, Hakim Naceur, Daniel Coutellier, and Abdel Laksimi. Geometrically nonlinear analysis of two-dimensional structures using an improved smoothed particle hydrodynamics method. *Engineering Computations*, 32(3):779–805, jan 2015.

- [55] Jiandong He, Nima Tofighi, Mehmet Yildiz, Juanmian Lei, and Afzal Suleman. A coupled wc-tl sph method for simulation of hydroelastic problems. *International Journal of Computational Fluid Dynamics*, 31(3):174–187, 2017.
- [56] J.J Monaghan and R.A Gingold. Shock simulation by the particle method sph. *Journal of Computational Physics*, 52(2):374–389, 1983.
- [57] David Kamensky, Georgios Moutsanidis, and Yuri Bazilevs. Hyperbolic phase field modeling of brittle fracture: Part I—Theory and simulations. *Journal of the Mechanics and Physics of Solids*, 121:81–98, 2018.
- [58] Gerhard A Holzapfel. Nonlinear solid mechanics: a continuum approach for engineering science. *Meccanica*, 37(4):489–490, 2002.
- [59] Michael J Borden, Thomas JR Hughes, Chad M Landis, Amin Anvari, and Isaac J Lee. A phase-field formulation for fracture in ductile materials: Finite deformation balance law derivation, plastic degradation, and stress triaxiality effects. *Computer Methods in Applied Mechanics and Engineering*, 312:130–166, 2016.
- [60] J. J. Monaghan. Smoothed particle hydrodynamics. *Annual Review of Astronomy and Astrophysics*, 30(1):543–574, 1992.
- [61] L. Brookshaw. A method of calculating radiative heat diffusion in particle simulations. *Publications of the Astronomical Society of Australia*, 6(2):207–210, January 1985.
- [62] T.N. Bittencourt, P.A. Wawrzynek, A.R. Ingraffea, and J.L. Sousa. Quasi-automatic simulation of crack propagation for 2d lefm problems. *Engineering Fracture Mechanics*, 55(2):321–334, 1996.
- [63] M. Naqib Rahimi, Adnan Kefal, Mehmet Yildiz, and Erkan Oterkus. An ordinary state-based peridynamic model for toughness enhancement of brittle materials through drilling stop-holes. *International Journal of Mechanical Sciences*, 182(May), 2020.
- [64] M. Naqib Rahimi. Peridynamic modelling of internal features and interfaces for material toughening. Master’s thesis, Sabanci University, dec 2020.
- [65] JF Kalthoff and S Winkler. Failure mode transition at high rates of shear loading. *DGM Informationsgesellschaft mbH, Impact Loading and Dynamic Behavior of Materials*, 1:185–195, 1988.

- [66] Adem Candaş, Erkan Oterkus, and Cevat Erdem İmrak. Dynamic Crack Propagation and Its Interaction With Micro-Cracks in an Impact Problem. *Journal of Engineering Materials and Technology*, 143(1), 08 2020.
- [67] Yousef Navidtehrani, Covadonga Betegón, and Emilio Martínez-Pañeda. A unified abaqus implementation of the phase field fracture method using only a user material subroutine. *Materials*, 14(8):1–19, 2021.
- [68] M. Naqib Rahimi, Adnan Kefal, and Mehmet Yildiz. An improved ordinary-state based peridynamic formulation for modeling FGMs with sharp interface transitions. *International Journal of Mechanical Sciences*, 197(December 2020):106322, 2021.
- [69] Florin Bobaru and Guanfeng Zhang. Why do cracks branch? A peridynamic investigation of dynamic brittle fracture. *International Journal of Fracture*, 196(1-2):59–98, 2015.
- [70] Rui Yan, Yong qiang Bi, and Wei Jiang. Simulation of contact interface between elastic solids using smoothed particle hydrodynamics. *Computational Particle Mechanics*, 9(1):167–177, 2022.